Diamond MEMS: from classical to quantum

*Huanying Sun, Zilong Zhang, Yulong Liu, Guo Chen, Tiefu Li†, Meiyong Liao**

Dr. Huanying Sun, Dr. Yulong Liu, Dr. Tiefu Li
Beijing Academy of Quantum Information Sciences, Beijing 100193, China
Dr. Tiefu Li
School of Integrated Circuits and Frontier Science Center for Quantum Information, Tsinghua University, Beijing 100084, China
Email Address: litf@tsinghua.edu.cn
Dr. Zilong Zhang, Mr. Guo Chen, Dr. Meiyong Liao
Research Center for Materials Center, National Institute for Materials Science, Namiki 1-1, Tsukuba, Ibaraki 305-0044, Japan
Dr. Meiyong Liao
Email Address: Meiyong.LIAO@nims.go.jp

Keywords: *Diamond MEMS resonator, NV center, Quantum sensor, spin-strain interaction, optomechanics*

Diamond has numerous outstanding properties in mechanics, physics,chemistry, electronics, thermodynamics, and spintronics for either classic micro/nano electromechanical systems (MEMS/NEMS) devices or hybrid quantum MEMS/NEMS systems. The extremely high mechanical strength and the ultra-wide bandgap energy enable the development of mechanically and thermally robust MEMS/NEMS sensors and switches, while the long coherence time of spin defects center enables the reading out through optical methods, precise quantum sensing, and quantum information processing. In this paper, the development of diamond-based MEMS/NEMS from the viewpoints of classic devices to quantum systems are reviewed. We firstly describe the fabrication process and the classic applications of diamond MEMS/NEMS devices, including those from micro-crystalline, nano-crystalline/ultranano-crystalline, and single-crystalline diamonds. Then, we introduce the physical properties of nitrogen-vacancy defect center, as well as the application referred to the hybrid system composed of MEMS structures and nitrogen-vacancy centers embedded, strain-spin interaction, and diamond-based optomechanics. Finally, a conclusion and outlook are presented. It is expected that diamond MEMS/NEMS is not only an ideal platform for high-performance and high-reliability advanced classic MEMS devices but also for quantum sensing, information, and exploring the fundamentals of quantum mechanics.

1 Introduction

Microelectromechanical/nanoelectromechanical systems (MEMS/NEMS) display important application prospects in various fields, including sensing, actuation, biomedicine, communication, and quantum technology, due to their advantages of small size, high sensitivity, lower power consumption, and integrability with modern electronics. As the key component of MEMS/NEMS, the realization of micro-nano mechanical resonator is aided by the development of modern complementary metal-oxide-semiconductor technology. When the frequency of an external stimulus matches the resonant frequency of a micro-nano mechanical resonator, the vibration of the mechanical structure reaches the maximum amplitude, known as the resonance state. Through electrical and/or optical measurement methods, such as capacitive coupling and optical interference, the change in resonant state of the MEMS/NEMS resonator due to external small stimulus can be measured, thereby realizing the measurement of extremely weak variables, such as the detection of gravitational waves [1], atomic mass [2], and single spin [3]. By using electrical signal input as a control method, the micro-nano mechanical resonator can be used as an actuator, such as a micro-motor, micro-valve, and micro-relay, etc. The micrometer size and high sensitivity of MEMS devices allow accurate medication delivery to desired locations in vivo or detection of diseased cells [4, 5]. High-frequency and high-quality (Q) factor MEMS resonators have significant potential in the development of high-sensitivity and high-resolution sensing devices and in the preparation of macroscopic quantum states [6, 7, 8, 9]. With advances in micro-nano fabrication processing technology, the decay time and resonant frequency of micro-nano mechanical oscillators have been significantly improved, providing important application prospects for higher-precision measurement as well as quantum information.

Diamond has drawn extensive attention as a material for micro-nano mechanical resonators due to its excellent mechanics, chemical inertness, biocompatibility, the highest thermal conductivity, high thermal stability, and low intrinsic dissipation [10, 11, 12]. Diamond-based MEMS can achieve the classic functions that Si MEMS have, but with superior reliability, longevity, and improved performance. Diamond MEMS has found various applications such as high temperature magnetic sensor [13], radio-frequency switch [14, 15], actuator [16], and high-frequency filters [17, 18]. Additionally, point defects such as nitrogen-vacancy center (NV center) in diamond is an ideal quantum object with long coherent time and can be easily initialized and readout optically [19]. Quantum devices based on NV center have a broad of applications, such as long-term data storage [20, 21], magnetic sensing [22, 23, 24], nanoscale thermometry [25], and quantum simulation [26, 27]. By combining the distinctive field sensitivity of NV centers and the nanometric spatial resolution intrinsic to atomic force microscope (AFM) cantilevers, this system could potentially facilitate quantum sensing of magnetic phenomena at ambient conditions. Furthermore, the strain coupling to NV centers generated by a MEMS resonator provides an additional degree of freedom to manipulate the spin states and a novel hybrid quantum system to engineering the strain-spin interaction [28, 29]. Due to the excellent mechanical properties and the low intrinsic dissipation of diamond MEMS, the preparation of macroscope quantum state has promising applications in quantum information processes as well as the fundamental exploration in quantum mechanics through the opto-phonon-spin system. The outstanding mechanical and spin properties of diamond bestow it a unique material for either classic or quantum applications based on diamond MEMS/NEMS resonators, as shown in Figure 1.

In this review, we predominantly focus on the potential applications of diamond-based MEMS resonators within both classical and quantum domains, with a specific emphasis on the mechanical motion of the resonator. This review is organized as follows. In Section 2, we give an overview of the development of diamond MEMS/NEMS resonators, covering the fabrication processes of resonator structure based on the micro-crystalline, nano-/ultranano-crystalline, and single-crystalline diamonds. Section 3 is dedicated to discussing the dissipative mechanism that impacts the quality factor of a resonator. In the Section 4, we present the applications of diamond MEMS devices with the three types of crystals mentioned above. The quantum applications related to the mechanical motion here are concentrated on the modulation of NV centers as well as the macroscopic quantum state of diamond MEMS resonator. In Section 5, we introduce the physical properties of NV centers and the corresponding Hamiltonian when interacting with other systems. The system architectures and their applications in the quantum domain with centering on diamond MEMS resonators are delineated below. Section 6 presents the hybrid system of NV centers embedded on the tip of an atom force microscopy cantilever; Section 7 explores the strain modulation of NV centers based on diamond beams; and Section 8 discusses the macroscopic quantum state based on the cavity optomechanics. Finally, we give a conclusion and a perspective in Section 9.

2 Microfabrication of diamond MEMS

During the past thirty years, the growth of diamond has gained a steady development due to the great advances in the chemical vapor deposition (CVD) methodology and the expanding application requirements in electronics [30], photonics [31], communications [32], sensors [33], and thermal managements [34]. In viewing of the progress of diamond growth and micromachining technologies, different diamond forms such as microcrystalline diamond (MCD), nanocrystalline diamond (NCD), and ultranano-crystalline diamond (UNCD), and single-crystalline diamond (SCD) were developed to fabricate diamond MEMS devices [14, 35, 36, 37, 38, 39, 40, 41, 42].

2.1 Micro-crystalline diamond MEMS

In the early 1990s, diamond-on-Si technology was proposed to achieve MCD-based MEMS resonators *via* the standard photolithography, thermal oxidation of silicon, and release of the diamond resonators by either anisotropic etching of silicon or SiO_2 [35]. In this process, the MCD film was grown on a Si

substrate by a microwave plasma-assisted CVD system. The resonator patterns were determined by the photolithography technique. The backside etching of the Si was utilized to release the resonator structure. Based on this method, various microstructures of membranes/windows, bridges, and cantilever beams of MCD were fabricated. In addition, the diamond-on-Si technology was further developed in fabricating MCD diamond-based MEMS resonators with high Q factors. Sepúlveda et al. reported the MCD-based resonators with a Q factor as high as 116 000 [43]. Figure 2 shows the fabrication process flow and the scanning electron microscopy (SEM) image of the MCD based cantilevers. In this method, the formation of a 2-μm thick SiO_2 layer on an n-type (100) Si wafer was the first step. The SiO_2 layer was used to act as the sacrificial layer to form the gap between the MCD and the Si substrate. Before the CVD diamond growth, the SiO_2/Si substrate was coated with a seeding layer of diamond powders to improve the nucleation density. The MCD was grown through the MPCVD method. Then, an aluminum (Al) layer was deposited on the MCD film to act as an etch mask assisted by photolithography patterning. The radio-frequency (RF) reactive ion etching (RIE) system with the oxygen-based plasma was utilized to etch the patterned MCD film. After dry etching, the Al etch mask layer was removed and the cantilevers were released by the wet etching in the HF acid. This microfabrication technology is a continuation and development of MCD MEMS technologies of previously reported [44, 45, 46].

2.2 Nano-/ultranano-crystalline diamond MEMS

The advantages of MCD/NCD/UNCD for MEMS are the large-wafer size, low cost, and compatible with Si technology. Conventional CVD film deposition techniques result in MCD films with large grains, high internal stress, poor intergranular adhesion, and rough surfaces, which limited MEMS applications [47]. The as-deposited NCD/UNCD films have small grain sizes in nanoscales (2-100 nm), smooth surface, a low coefficient of friction (COF) (0.02-0.05), a high hardness (98 GPa), and Young's modulus (980-1120 GPa) similar to those for SCD [37, 38, 47, 48, 49, 50]. A low COF is crucial in MEMS technology since the lubrication is one of the main constraints for MEMS devices. The conventional techniques for providing lubricant to the interface between contacting parts are highly challenging to accomplish. Due to the unique morphological, mechanical, and tribological properties, NCD/UNCD films are promising materials for the development of high-reliability and long-term MEMS devices. A mass of efforts have been made in the microfabrication processes for producing NCD/UNCD-based MEMS devices [37, 49, 51, 52]. The mainstream route of the fabrication flow can be summarized as a serial of steps, which involves: (1) surface oxidation of a Si substrate to form a sacrificial oxide layer, (2) surface seeding with diamond powders and subsequent CVD growth of NCD/UNCD films on the SiO_2/Si substrate, (3) deposition of a metal layer on the as-grown NCD/UNCD films as the etching mask and lithography patterning, (4) RIE dry etching of the NCD/UNCD films through the mask, and (5) wet etching (acid etching) to remove the sacrificial SiO_2 and the metal mask to release the MEMS device structure. The main microfabrication methods of the NCD/UNCD-based MEMS devices are similar to those of the MCD-based MEMS devices.

2.3 Single-crystalline diamond MEMS

Compared to SCD, polycrystalline diamonds (PCDs) including MCD and NCD/UNCD suffered from the disadvantages of many grains and grain boundaries, impurities, and limited control over their properties, which leads to high internal loss, inferior electronics properties, and the degradation in reliability [53, 54]. SCD can make full use of the ultimate properties of diamond in every aspect for MEMS application with high performance and high reliability. In addition, SCD offers a platform for defect spin centers such as NV centers to achieve long quantum coherence times [55], which makes it promising for quantum applications involving a MEMS resonator coupled with a spin center [56, 57]. Therefore, SCD is an ideal material for either classic MEMS sensors or quantum devices. With the great progress of the growth techniques and micromachining techniques for SCD, a serials of microfabrication methods for SCD-based MEMS have been developed. The main approaches for SCD-based MEMS resonators can be described as three categories: (1) smart-cut method through ion-implantation assisted lift-off (IAL)

technology [39, 58, 59], (2) bonding a SCD plate on an insulator substrate to form diamond-on-insulator (DOI) structure and reducing the SCD plate to the desired thickness [60, 61], and (3) diamond thinning through anisotropic plasma etching (APE) [62, 63]. These above methods were discussed in details in related works [64, 54]. The smart-cut technique was initially proposed by Parikh et al. for freestanding diamond plate preparation [65]. The smart-cut process involved directly manufacturing devices on a thick SCD substrate. The ion implantation was the unique step to produce an ion-damaged graphite-like layer buried in the diamond substrate, which acted as the sacrificial layer in the later release step. The sacrificial layer was then selectively removed to release the desired device structure. By inspiring idea from the microfabrication of freestanding diamond plate, the smart-cut technique was greatly developed for fabricating various SCD MEMS structures [14, 39, 58, 54, 53]. The smart-cut method is in favor of achieving SCD MEMS devices with the SCD-on-SCD structure, controlled dimensions from nanoscale to microscale, high reproducibility, and high reliability.

In the APE technology, designed patterns were firstly obtained based on the standard photolithography, then, SCD was etched by RIE through the protection mask. Finally, an anisotropic plasma etching was performed at an oblique angle to the substrate surface. The angled-etching produced freestanding nanobeams with triangular cross-sections directly from SCD substrates [62]. The APE process contributes to integrating photonic and MEMS structures in SCDs. The DOI technique involved bonding diamond onto a foreign substrate and thinning the SCD to a desired thickness by the mechanical polishing treatment and the RIE etching. The desired device structure was then released by removing the oxide [60, 61, 66]. The DOI method facilely realized the high Q factors diamond MEMS resonators.

3 Energy dissipation mechanisms of diamond MEMS

For a MEMS resonator, resonance frequency and Q factor are the most important parameters to characterize the fundamental performance. The resonant frequency is primarily determined by the geometrical dimensions, structural material properties, stress, and surface topography [67]. The resonant frequency is not only critical to characterize the resonance vibration performance of MEMS devices, but also have an important impact on the functional performances [68]. For the diamond MEMS devices with the transverse dimensions (i.e. thickness and width) much smaller than the longitudinal dimension (i.e. length), the vibrational motion is governed by the flexural motion. The resonance frequency of the diamond MEMS can be described and analyzed by the Euler-Bernoulli theory [67, 68, 69],

$$f_r = k\frac{t}{L^2}\sqrt{\frac{E}{\rho}} \tag{1}$$

where t, L, E and ρ are the thickness, the length, the Young's modulus, and the mass density of the diamond resonator, respectively. k is a parameter depending on the vibration mode and the resonator structure. For the resonator beam with the clamp-free structure, k are equal to 0.162, 1.014, 2.840, $\cdots$, respectively (corresponding to the first mode, the second mode, the third mode, respectively). For the resonator beam with the clamp-clamp structure, k are equal to 1.028, 2.289, 5.564, $\cdots$, respectively (corresponding to the first mode, the second mode, the third mode, $\cdots$, respectively).

3.1 Energy dissipation mechanism for diamond resonators

The Q factor, the inverse of the dissipation, is a key figure of merit for a MEMS resonator. It is defined as a measure of the energy lost (ΔW) in one radian of the cycle of oscillation as a fraction of the total mechanical energy (W_0) of the resonator. A higher Q factor means a lower rate of damping or energy losses. The Q factor can be expressed as [70],

$$Q^{-1} = \frac{\Delta W}{2\pi W_0} \approx \frac{\Delta f_r}{f_r} \tag{2}$$

where f_r is the resonance frequency. Δf_r is the full width at half maximum (FWHM) of the resonance vibration spectrum through the Lorentzian curve fitting. The first term in the expression is the standard definition of dissipation. The latter expression is obtained by solving the standard damped resonator equation. It is dislocated that a high Q factor enhances the vibrational amplitude at resonance frequency and reduces the resonance peak width. In viewing of various energy dissipation mechanisms, the overall Q factor of a resonator is expressed as [64, 70, 71],

$$Q^{-1} = Q^{-1}_{\text{clamp}} + Q^{-1}_{\text{surface}} + Q^{-1}_{\text{TED}} + Q^{-1}_{\text{air}} + Q^{-1}_{\text{bulk}} + \cdots \tag{3}$$

where Q^{-1}_{clamp}, Q^{-1}_{surface}, Q^{-1}_{TED}, Q^{-1}_{air}, and Q^{-1}_{bulk} represent the energy dissipation from clamping loss, surface loss, thermoelastic damping (TED), air damping, and bulk defects, respectively. For diamond MEMS resonators made through various microfabrication methods, the Q factors were primarily determined by the comprehensive energy dissipations. For example, the bulk defects and surface effect dissipation have a vital impact on the Q factors of the diamond MEMS resonators fabricated by the smart-cut technique [59, 72]. A high Q factor is desirable for diamond MEMS resonators for sensing application with high sensitivity and low noise. To have a high-speed operation, a high resonance frequency is also pursued. Therefore, a trade-off between the resonance frequency and the Q factor need to be considered.

4 Diamond MEMS devices

4.1 Micro-crystalline diamond-based MEMS devices

Due to the exceptional properties of diamond, such as its high mechanical strength, chemical inertness, excellent thermal conductivity, and wide bandgap, MCD material offers unique advantages in MEMS applications compared to that of Si material [41]. With ongoing research and advancements in MCD deposition techniques and microfabrication methods, the utilization of MCD in MEMS applications are greatly broadened and developed. The applications of MCD MEMS devices are across a wide range of applications, mainly including sensing [73, 74, 75], RF MEMS [76], microfluidics [77, 78, 79], and optics [80, 81]. MCD MEMS was developed for sensors and actuators, such as pressure sensing, gas sensing, and gyroscopes [82]. The high thermal conductivity of MCD enables efficient heat dissipation in RF devices for high-power handling. Additionally, the low dielectric constant and loss tangent of diamond contribute to low signal loss and high Q-factor in resonant structures. MCD based microfluidics can withstand harsh chemical environments and provide excellent resistance to befouling. In addition, the MCD microfluidic channel offered an useful component to extract thermal energy from microelectronics circuits [79]. However, among diamond materials, the grain size of MCD in several micrometers could lead to the increase in the important propagation losses, which limited MCD MEMS in the applications of acoustic propagation [41]. The MCD exhibits a certain level of surface roughness, which affects the performance of MEMS devices, particularly in applications where smooth and uniform surfaces are required. Additional processing steps or surface treatments are necessary to achieve the desired surface quality.

It is worth noting that the MCD MEMS devices are still evolving, and further research is being conducted to explore new application fields,devices design,and performance improvement. The above-mentioned issues can be circumvented through the NCD/UNCD and SCD, which promote the further development of diamond MEMS devices with high performance and high reliability.

4.2 Nano-/ultranano-crystalline diamond-based MEMS devices

Over the last three decades, NCD and UNCD films have been used as structural materials in many MEMS applications [48, 51, 83, 84, 85, 86, 87, 40, 88, 89]. The MEMS devices made from NCD and UNCD films mainly include the UNCD- and NCD-based resonators [48, 51, 87, 40], the UNCD-based scanning probe microscopy (SPM) and atom force microscopy (AFM) tips [85, 88, 89], and the UNCD-based RF MEMS-switches [86, 90, 91]. The NCD-based micromechanical disk resonator was demonstrated, exhibiting a record frequency of 1.51 GHz with a high Q factor of 11 555, 7 orders of magnitude higher

than the previously demonstrated 1.14-GHz polysilicon disk resonator [92]. The optical resonators based on the NCD were developed to offer a platform for micro/nanophotonic devices with embedded diamond color centers [87]. Figure 3(a-c) show the NCD based microcavity resonator and the stimulation of Q factors influenced by the distance between the disk and substrate. The three-dimensional finite-difference time-domain (FDTD) was utilized to figure out the expected mode profiles and the high Q factors. In the microdisk, the Q factor was limited by the absorption and scattering in the NCD material. RF-MEMS is one of the important components in Radar and mobile communication electronics. An RF mechanical resonators array based on the NCD material was fabricated (Figure 3(d)) [51]. The modes of the NCD resonator array unit cell were analyzed, showing the larger splitting of the array modes, the stronger the coupling of the array (Figure 3(e-f)). The high Q factors of the NCD resonators create opportunities for implementing various devices for RF communication such as broad band filters, delay lines, and frequency analyzers.

Due to that the charging and discharging time constants are 5-6 orders of magnitude faster than those of conventional insulating dielectric films using dielectric layers such as SiO_2 and Si_3N_4, UNCD shows a great potential in the capacitive RF MEMS switch as the dielectric without the adverse effect on switch reliability [93]. For the first time, the integration UNCD RF-MEMS switch with SOS (silicon-on-sapphire)-CMOS device was fabricated through the microfabrication steps, including patterning, photolithography, deposition, reactive-ion etching (RIE), and chemical etching [93]. The RF-MEMS capacitive switch involves a flexible metal membrane dangling over a lower metal electrode coated with a UNCD dielectric layer, as shown in Figure 4(a). Figure 4(b) and (c) exhibit the cross-section view of the RF-MEMS switch with the UNCD as the dielectric layer and the optical image of the RF-UNCD/MEMS switch in integrated with the CMOS device, respectively. As applying an electric field between the metal membrane and the lower electrode, the motion of the membrane could lead to the change of membrane/electrode capacitance, generating the RF signal [93]. When the electric field was turned off, the membrane disconnected with the UNCD/electrode, breaking off the RF signal. The RF performance of the RF-UNCD/MEMS switches was investigated by the electrical measurements. The enhanced reliability of the RF-UNCD/MEMS switch was achieved due to the hydrophobic nature of the UNCD film surface. The work suggests a new paradigm of operation of UNCD MEMS that potentially mitigates the dielectric charging hazard and stiction issues. It is noted that the high film stress and the structure delamination issues should be solved out before the commercial application of the RF-UNCD/MEMS switches.

4.3 Single-crystalline diamond-based MEMS devices

Recently, there had been a remarkable progress in the utilization of SCD as a material in various fields such as, micromechanics, nanophotonics, quantum information, and sensors since SCD material hosts the exceptional mechanical properties, extensive optical transparency, and biocompatibility [94]. The advancement in high-crystal-quality SCD growth methods and nanofabrication technologies contribute to the development of SCD MEMS.

SCD resonators allow to achieve high performance in force sensing [95, 96, 97], mass sensing [66, 98], gas sensing [99, 100], pressure sensing [53], smart electrical switch [14], and optomechanical systems coupling the optical mode with mechanical modes [101, 102]. The NEMS switch has emerged as a prospective alternative to the complementary metal oxide semiconductor (CMOS) technology. However, the existing MEMS switches utilizing silicon technologies encounter challenges such as stiction, abrasion, weak mechanical and tribological characteristics, which adversely affect the reliability of the electrical contacts [103, 104]. SCD is a promising choice to fabricate NEMS switches with excellent contact reliability. In 2010, the first SCD NEMS switch was fabricated, as shown in Figure 5 [14]. Figure 5(a-c) show the structure of the switch with the off-state. The control mechanism of the switch was that when applying voltages on the source and the gate, the SCD cantilever deflected due to electrostatic attraction, creating an electrical contact at the drain, thus achieving the conducting state (on-state). As the voltages were turn off, the SCD cantilever was disconnected from the drain, thereby achieving the off-state. It is disclosed that the pull-in voltage exhibits the weak dependence on the gate voltage, which confirm-

s the mechanical switch behavior for the SCD NEMS switch (Figure 5(d-e)). Figure 5(f) exhibits the good transient switching performance of the switch. The SCD MEMS switch had extremely low leakage current (< 0.1 pA) and high on/off ratio of more than 6 orders of magnitude. In addition, the power consumption of the switch in the off-state was calculated as less than 1 pW. The developed SCD NEMS switches has the potential to serve as microwave switches in next-generation wireless communications and logic circuits, even in harsh environments. The NEMS switch was the firstly movable SCD MEMS/NEMS devices, which has established the infrastructure for a variety of SCD MEMS/NEMS for the development of diverse chemical, physical, and mechanical sensors. The smart cut method involves an ion implantation process that creates damage in the SCD substrate (the bottom of the SCD MEMS resonator). The Q factors were thus at the level of several thousands. By growing thick SCD homoepitaxial layer or removing the bottom damage diamond layer, the Q factors were increased by over 10 or 100 times [59, 105]. The Q factor as high as 1 million was obtained by the smart-cut method, the same as those of fabricated by DOI method started from a SCD plate [66].

Due to high thermal stability and mechanical robustness, SCD MEMS was applied for high temperature sensors. One example is pico-thermo gravimetric analysis of material properties using diamond cantilever beam. The thermal decomposition of calcium carbonate ($CaCO_3$) was investigated from room temperature to 600 °C [106]. By analysing the temperature dependent resonant frequency behavior, the thermal conversion from $CaCO_3$ to CaO starts around 500 °C was identified. The SCD cantilevers offer a novel thermogravimetic technique for accurate information about the analyzed material at picogram range during the thermal process. Another example of SCD MEMS is the high-temperature magnetic sensor. By depositing a magnetrostrictive FeGa thin film on the SCD cantilever, the external magnetic fields can be detected based on the resonance frequency shift [107]. Since both FeGa and SCD MEMS have high thermal stability, high-temperature SCD MEMS magnetic sensor were developed operable up to 500 °C [108]. The SCD MEMS magnetic sensor showed a noise level of 10 $\mathrm{nT}/\sqrt{\mathrm{Hz}}$.

For a SPM, non-contact friction exists between the probe tip and the measured sample surface [97], which arises from the dissipative forces between the moving tip and the surface. This non-contact friction degrades the force sensitivity. These factors include dielectric fluctuations, radiative heat transfer, and the existence of static or fluctuating surface charge [109, 110]. SCD processes a remarkably low dielectric constant and minimal loss tangent, thereby making it an excellent choice for a low-friction tip material. Additionally, the exceptional mechanical durability and high wear resistance of diamond make it a highly desirable option for force microscopy, addressing crucial practical concerns. The ultrasensitive force microscopies, consisting of SCD nanowires integrated on the ends of silicon cantilevers were fabricated [97]. Figure 6(a) shows a SCD nanowire tips attached on a cantilever. The noncontact friction of SCD nanowire tip is measured through using a pendulum configuration, as illustrated in Figure 6(b). The SCD nanowire tip was controllably approached to a gold surface via a piezo-driving position stage. The ring-down method was utilized to measure the Q factor of the integrated cantilever. It is disclosed that the little changes in Q factors occurred until the tip-surface distance decreased to below 10 nm (Figure 6(c)). In addition, even when approaching the surface ($z \approx 1$ nm), the Q factor remains consistently as high as 40 000. It was found that the SCD nanowire tip had extremely low values of noncontact friction, about 3×10^{-15} kg/s at $z = 10$ nm and 9×10^{-15} kg/s at $z = 5$ nm (Figure 6(d)), much lower than that of Si tip. The result indicated the SCD nanowire tips were feasible without no deterioration in force sensitivity as z lower than 10 nm. The minimum detectable force, $S_F^{1/2}$ of the SCD nanowire-tipped cantilever reached a very low value of 2.4 $\mathrm{aN/Hz^{1/2}}$ at $z = 10$ nm for $T = 4$ K (Figure 6(d)). Furthermore, the minimum detectable force was improved to be $S_F^{1/2} \approx 0.65$ $\mathrm{aN/Hz^{1/2}}$ as the measured temperature $T = 300$ mK. Due to the high force sensitivities, the SCD nanowire-tipped cantilevers present a useful platform for measuring friction of single nano-objects, like large biomolecules or quantum dots.

5 Nitrogen-vacancy defect center

Before introducing the hybrid MEMS quantum system, the nitrogen-vacancy (NV) center is briefly described. The NV center is a type of defect in diamond that occurs when a nitrogen atom replaces a carbon atom and an adjacent vacancy is created in the diamond lattice. It was discovered by du Preez in 1965 [111] and has now gained considerable attention for quantum science and technology. The NV center exhibits exceptional optical and spin properties, making it ideal for a variety of applications, such as quantum sensing, quantum simulation, magnetometery, and biology imaging. Additionally, an NV hybrid system has emerged as a promising tool for fundamental physical studies such as quantum coherence and entanglement.

The typical charge state of NV center are the negative charged state of NV^- and neutral charge state NV^0. The former is composed of six electrons, with five provided by the dangling bonds of the nearest carbons and nitrogen atom and the sixth captured from the nearby substitutional nitrogen. The latter is constructed by the mentioned five electrons, thereby maintaining electrical neutrality [112]. Although both NV^0 and NV^- have been the subject of extensive study, greater attention has been devoted to the negatively charged NV center due to its unique capability of optical initialization and readout of spin state [113, 114, 115, 116]. In this review, we focus on the negatively charged NV center and refer to as NV center unless specified otherwise.

The atom structure of NV center has the trigonal symmetry of point group C_{3v}, in which its principle axis is aligned with the crystallographic $\langle 111 \rangle$ direction. Figure 7(a) illustrates the atomic structure of the NV center[117]. The elements of C_{3v} group are defined with respect to the trigonal symmetry axis and can be categorized as one of the three classes: the identity element (e), the C_3 rotations about the symmetry axis, and the vertical reflections (σ_v) through the planes that includes the symmetry axis. The C_{3v} group, with three classes, can be described by three irreducible representations: A_1, A_2 and E, which are of dimensions one, one, and two, respectively [118].

The electronic structure of NV center is confirmed to be localized around the vacancy site by electron paramagnetic resonance measurement [119, 120]. As such, the wavefunction of the NV center can be described by a molecular orbital model, which is a linear combination of atomic orbitals. The atomic orbitals, being of the tetrahedrally coordinated sp^3 orbitals, constitute the basis function of molecular orbital model. Ab initio calculation have determined the molecular orbitals of the ground state and the first excited state, revealing that three orbitals are located in the band gap (a_1, a_x, a_y), while one is in the valence band (a_1') [121, 122]. The spatial distribution of molecular orbitals and the electronic occupancy of ground and excited states are shown in Figure 7(b).

5.1 Energy levels and polarization properties of NV center

The NV center has a spin-triplet state with electronic configuration $^3A_2(a_1^2e^2)$ for the ground state and $^3E(a_1e^3)$ for the first excited state. There are two intermediated singlet states between the ground state and first excited state [123]. The electronic structure of the NV^- at room temperature is shown in Figure 7(c). The ground state and excited state are spin triplet (S=1) and are split into three spin sublevels ($m_s = 0, m_s = \pm 1$) due to the spin-spin interaction between the unpaired electron and nitrogen nuclei in the diamond lattice. The property of the NV center can be characterized by the energy difference between the spin sublevels of the spin triplet state, corresponding to $D_{gs} = 2.87$ GHz for the ground state and $D_{es} = 1.42$ GHz for the excited state, where D is the so-called zero-field splitting (ZFS) [124]. The strength of the ZFS is dependent on the orientation of the NV center with respect to the crystal axes of the diamond, resulting in an anisotropic splitting [125, 126]. The transition rates between the $m_s = 0$ and $m_s = \pm 1$ sublevels are used to determine the spin-lattice relaxation time T_1, which is typical a few milliseconds at room temperature [127]. The degeneracy of the triplet states can be lifted by the magnetic field via Zeeman effect, which causes the levels of the $m_s = \pm 1$ to shift in opposite directions (Figure 7(c), inset). The dependence of the energy shift on the magnetic field is the

foundation of the NV center-based magnetic field sensors. The spin polarization and transitions between ground state and the excited state are typically achieved by the non-resonance laser excitation at 532 nm, with the corresponding spontaneous emission at 637 nm and 1042 nm being also the identified features of NV^- [128, 129].

One of the advantage of NV center is the efficient initialization and readout of NV spin states via the optical method. The energy levels and the decay pathways are displayed in Figure 7(c). Under the non-resonant optical excitation, the NV center experiences a transition from the ground state $^3A_2$ to the excited state ^3E, followed by transitions to either the ground state directly or via the intermediate singlet states $^1A_1$ and ^1E. Except for the infrared ZPL at 1042 nm, the transition processes that occur also by virtue of the intermediate singlet states are non-radiative. The non-radiative decay rates depend on the spin sublevel, with the decay rate for $m_s = \pm 1$ being faster than that of $m_s = 0$ during the transition from excited state ^3E to intermediate state $^1A_1$, and the decay rate about the non-radiative transition from the dark state ^1E to the $^3A_2$ is similar for both sublevels [130, 131, 27, 132]. After multiple cycles, the state of the NV center will end up in the $m_s = 0$ ground state, regardless of whether it started in $m_s = 0$ or $m_s = \pm 1$. Additionally, the fluorescence intensity could be used to determine the spin state since the alternate decay path does not emit a photon in the fluorescence band. It was reported that the fidelity of $m_s = 0$ was up to 96% under the non-resonant excitation [133]. If resonant excitation is implemented, the expected spin state can be prepared, and the fidelity can be enhanced. It was demonstrated that the fidelity were up to 99.7% and 99.2% for spin $m_s = 0$ and $m_s = \pm 1$, respectively [134]. These processes enable the initialization of the quantum state of a qubit for quantum information processing or quantum detection.

5.2 Fabrication of NV centers

High-quality NV centers are essential for the development of powerful and efficient NV-center based quantum devices, such as sensors and qubits for quantum computing. Methods for generating diamond typically involve CVD and detonation synthesis [135]. The creation of NV centers in the diamond involves two processes: the introduction of a substituted nitrogen atom and the adjacent vacancy. Nitrogen atoms can be implanted into the pure diamond substrate using the high energy nitrogen ions or introduced by adding nitrogen gas during the CVD growth of diamond. The approaches for introducing vacancies generally include the irradiation (e.g. electron, proton, neutron, and femtosecond laser [136, 137, 138, 139, 140]), or the impanation of additional ion species (e.g. He, Ni, C, Ga [141, 142, 143, 144]). During this process, the high energy particle beam interacts with the crystal lattice and has a certain probability of replacing the carbon atoms in the crystal lattice, hence the vacancies would be created in the lattice. The depth and the density of generated defects depend on the energy and the concentration of implanted ions. However, the efficiency of N-to-NV conversion is very low if only the nitrogen and the vacancies are introduced into the diamond. Therefore, an annealing treatment is often employed as a fallow-up process to facilitate the diffusion of nitrogen atoms and the migration of vacancies. This promotes the formation of the nitrogen-vacancy complexes and enhances the conversion efficiency of the complexes into NV centers by triggering a rearrangement of the atomic structure [145]. Annealing conditions, such as temperature, pressure, and time, strongly affect the physical properties of the resulting NV centers [141, 146, 147, 148].

NV centers in diamond are being developed with a focus on controlling their properties, enhancing scalability, and integrating them with other materials or system to expand their potential applications. The sensitivity and spatial resolution of NV center-based devices are intimately linked to their coherent time. In generally, the longer relaxation time, the greater the detection sensitivity and resolution. However, the length of the relaxation time is influenced by the surrounding environment. Optimizing the preparation conditions allows to extend the relaxation time, control the embedded depth, and manipulate the NV sites at the individual or population level. The scalability and the integrability of the NV centers enable the practical development of quantum technologies with applications in fields such as sensing, computing, communication, medicine, and energy. By using isotopically enriched methane

during CVD growth and extremely low concentration of nitrogen impurity ($< 5.2 \times 10^{-2}$ ppb), the dephasing time of single electron spins is over 1 millisecond at room temperature [149]. By using naturally isotopic abundance nanodiamonds produced by Si_3N_4 ball milling of CVD grown bulk diamond with an average single substitutional nitrogen concentration of 121 ppb, the electron spin coherence times of NV^- centers exceeding 400 μs at room temperature was achieved [150]. By combining ion implantation or CVD with photolithography technology, it is possible to fabricate large-scale NV centers and single NV centers or NV ensembles in desired patterns with MEMS/NEMS structures such as micro-cavities, nano-photonics and micro-circuits on a chip [151]. Hybrid systems utilizing NV centers can leverage the unique strengths of each subsystem to achieve optimal performance.

5.3 Optical detection of magnetic resonance

The investigation of electron configurations and magnetic characteristics of NV centers in diamond can be conducted by monitoring variations in spectroscopy in response to alterations in external magnetic and microwave fields. The two most common detection methods are electron paramagnetic resonance (EPR) and optical detection magnetic resonance (ODMR). The principle behind both techniques is based on the Zeeman effect in which the energy level of the NV centers will split due to the presence of a magnetic field, and the experimental setups for both techniques have many similarities. In EPR, the diamond sample with NV centers embedded is first placed in a strong static magnetic field, followed by the application of a microwave field that causes the electron transition between the ground state and excite state. The resulting change in electron spin state leads to the absorption of the energy at a specific resonance frequency, providing the information about the NV center's electron structure and magnetic properties. ODMR is the more commonly used technique, which involves shining the laser light on the NV centers and detecting changes in their fluorescence intensities as an external magnetic field is applied. A schematic of the ODMR experimental setup is given in Figure 8(a) [152].For optical excitation of NV centers, a single-mode, fiber-coupled collimated laser beam with a wavelength of 532 nm is employed. This laser beam is defocused via an achromatic lens to adjust the illuminating area to the focal plane. The photoluminescence (PL) signal from the NV centers is collected by an objective lens, transmitted through a dichroic mirror, filtered through a long-pass filter, and directed into the detection optics. A flip mirror within the detection optics presents two pathways: an imaging path to a CMOS sensor and a photon-counting path through intermediate optics to a single-mode fiber. A complementary electronic interface has been devised to regulate the excitation and subsequent readout of NV quantum centers. An field-programmable gate array (FPGA) device performs real-time analysis and the experimental parameters control with the implementations of a digital filter. The FPGA device converts transistor-transistor logic (TTL) pulses captured by a single-photon avalanche diode into the spin state-dependent PL signal, generates TTL pulse trains to synchronize excitation and detection units, and processes the acquired data of ODMR spectrum. Electron spin resonance is driven by frequency-modulated microwaves generated with a dual-channel radio-frequency (RF) signal source. The output is amplitude modulated by an RF switch and amplified before being sent through an RF waveguide and microwave antenna, accompanied by a circulator to prevent back reflections [152].

The use of ODMR to probe the NV centers has several advantages, including non-destructive to the spin states being measured [153] and highly sensitive detection, high spatial resolution capabilities, ease of implementation, and the ability to make measurements of the electronic spin state. Figure 8(b) shows a fluorescence scan of a single NV center, which exhibits a distribution of fluorescence intensity that fits well with the expected profile, indicating that there is no damage or alteration near the NV defect center area [154, 155]. The negative charge of NV^- is identified by the sharp zero phonon line at a wavelength of 637 nm [156], as depicted in Figure 8(c). To determine the number of NV centers at a particular location on a diamond sample, it is necessary to evaluate the photon statistics emitted at that location. This is achieved by measuring the normalized second-order autocorrelation function:

$$g^{(2)}(\tau) = \frac{\langle I(t) \cdot I(t+\tau) \rangle}{\langle I(t)^2 \rangle} \tag{4}$$

The quantity $g^{(2)}(\tau)$ measures the conditional probability of find a second photon at time τ, given the first photon was emitted at time zero. In a single quantum system, it is expected that $g^{(2)}(\tau)$ will drop to zero for very small values of τ. This phenomenon is commonly known as antibunching and essentially describes the fact that a single quantum system can only emit one photon at a time. In generally, if N defect centers are optically excited, the autocorrelation function could be provide by the formula [157],

$$g^{(2)}(\tau) = 1 + \frac{1}{N}(C_1 \cdot e^{-|\tau/\tau_1|} + C_2 \cdot e^{-|\tau/\tau_2|}) \tag{5}$$

here the parameters C_1, τ_1, and τ_2 are determined by the properties of the defect centers and the nature of excitation,such as the internal relaxation rates and excitation intensity. Specially, $C_2 = -1 - C_1$. Figure 8(d) provides examples of the autocorrelation function obtained for different numbers of NV centers [158]. The ODMR spectrum of a single NV^- at different magnetic field are shown in Figure 8(e) [159]. It depicts the splitting of the spectral lines is proportional to magnetic field strength, and the the drop of PL reveals the transitions from the $m_s = 0$ to $m_s = \pm 1$ states. As a result, the NV center has been studied as solid sources of single photons.

While both EPR and ODMR are effective in detecting NV centers, they have different strengthes and limitations, and their selection depends on the purpose of the study and the experimental conditions. EPR provides precise information on the spin state and electronic structure of NV centers and is suitable for studying the ensembles and the fast dynamics of NV centers. On the other hand, ODMR is highly sensitive and efficient for studying single NV center and extracting information about the magnetic properties of NV centers, such as spin number, spin decoherence, and relaxation times. Its limitations include low signal-to-noise ratio and the spatial resolution, which are limited by the optical diffraction limit. Nevertheless, ODMR remains an ideal technique for investigating individual NV center [160, 161, 162].

5.4 Hamiltonian

The development of NV center-based applications stems from their sensitive responses to the external circumstance. The Hamiltonian including the NV center and host nuclear spin can be expressed as:

$$\hat{H} = \hat{H}_S + \hat{H}_I + \hat{H}_{SI} + \hat{H}_B + \hat{H}_E \tag{6}$$

Where H_S describes the contribution from electron spin of $S = 1$, and H_I is related to the nitrogen spin of ^{14}N or ^{15}N with $I = 1$ or $I = 1/2$, respectively. The H_{SI} is the interaction between the electron spin and nuclear spin. H_B represents the interactions with the magnetic field, and H_E is the interactions with the electric field and strain. Each terms in Equation (6) can be described by (setting $h = 1$):

$$\hat{H}_S = D[\hat{S}_z^2 - S(S+1)/3] \tag{7}$$

$$\hat{H}_I = P[\hat{I}_z^2 - I(I+1)/3] \tag{8}$$

$$\hat{H}_{SI} = A^{\parallel}\hat{S}_z\hat{I}_z + A^{\perp}(\hat{S}_x\hat{I}_x + \hat{S}_y I_y) \tag{9}$$

The Hamiltonian for both the ground state and the excited state share the same form but with different parameters. The D parameter in H_S originats from the axial zero-field splitting with $D_{gs} = 2.87$ GHz for ground state and $D_{es} = 1.42$ GHz for excited state [124, 163]. The P parameter in the host ^{14}N nuclear spin Hamiltonian depends on the quadrupole splitting parameter, with $P_{gs} = -4.945$ MHz and an undetermined value for the excited state [164]. The P parameter for ^{15}N is zero because it is a system of spin 1/2. The axial and transverse components of the hyperfine constant are $A_{gs}^{\parallel} = 3.03$ MHz and $A_{gs}^{\perp} = 3.65$ MHz for ground state and $A_{es}^{\parallel} = 40$ MHz and $A_{ds}^{\perp} = 40$ MHz for excited state [165, 164].

The influence of magnetic field $\vec{B}$, static electric field $\vec{E}$ and the strain field $\vec{\delta}$ on the NV center can be described using the following Hamiltonians [166, 167]:

$$\hat{H}_B = g_s^{\parallel}\mu_B\hat{S}_z B_z + g_s^{\perp}\mu_B(\hat{S}_x B_x + \hat{S}_y B_y) + g_N\mu_N\hat{\mathbf{I}}\cdot\mathbf{B} \tag{10}$$

$$\hat{H}_{E,gs} = d_{gs}^{\parallel}(E_z+\delta_z)\left[\hat{S}_z^2 - S(S+1)/3\right] + d_{gs}^{\perp}(E_x+\delta_x)[\hat{S}_y^2 - \hat{S}_x^2] + d_{gs}^{\perp}(E_y+\delta_y)[\hat{S}_x\hat{S}_y - \hat{S}_y\hat{S}_x] \quad (11)$$

$$\hat{H}_{E,es} = d_{es}^{\parallel}(E_z+\delta_z) + g_{es}\hat{\mathbf{S}}\cdot\mathbf{B} + \xi[\hat{S}_y^2 - \hat{S}_x^2] \quad (12)$$

Here, $\mu_B = 9.27 \times 10^{-24}$ J/T is Bohr magneton and $\mu_N = 5.05 \times 10^{-27}$ J/T is the nuclear magneton. $g_s^{\parallel}$ and $g_s^{\perp}$ are the longitudinal and transverse ground state electronic g-factor, and are both close to the electron Landé factor with $g_s = 2.003$ [112, 164]. The isotropic nuclear g-factor is denoted by g_N, where $g_N = 0.4038$ for ^{14}N and $g_N = -0.5664$ for ^{15}N. $\hat{H}_{E,gs}$ and $\hat{H}_{E,es}$ are the Hamiltonian of ground state and excited state, respectively. The longitudinal and transverse components of the ground state electric dipole moment are $d_{gs}^{\parallel} \approx 0.35$ Hz cm/V and $d_{gs}^{\perp} \approx 17$ Hz cm/V [168]. $d_{es}^{\parallel}$ is the components of electronic electric dipole moment of ^{3}E state, and g-factor of ^{3}E is 2.01 at room temperature. ξ is related to strain and it represents the splitting caused by strain [169, 170]. It has been measured to be 70 ± 30 MHz in bulk diamond [163] with 5 MHz ground state strain splitting. The strain would cause the energy level splitting like the effect of electric field, which is induced due to the lattice displacement or deformation. Therefore, the strain could be a controllable degree of freedom to mediate the spin ensemble in the NV embedded micromechanical resonators. The Hamiltonian serves as the theoretical basis for constructing various sensors and quantum information devices.

6 Hybrid system of NV centers and MEMS

NV centers in bulk diamond has been thoroughly investigated for their applicability in the quantum sensing, quantum computing, biomedical imaging, and optoelectronics. In the next three sections, we will concentrate primarily on the potential applications of diamond-based MEMS resonators in the field of quantum region. More specifically, we will pay close attention to the applications of systems that consisting of AFM cantilever beams and NV centers, diamond MEMS resonators with embedded NV centers, and cavity optomechanics systems composed of diamond MEMS resonators and optical cavities.

By integrating NV centers with a cantilever in an AFM to form the hybrid system, one can extend the color centers in diamond for a variety of scanning probe applications [171]. The typical illustration of this hybrid system is shown as the centered in Figure 9 [172]. The NV centers are housed at the apex of the scanned cantilever tip. Optical excitation of the NV center is achieved by using a laser, while a microwave radiation is used to induce EPR transitions of the center. The frequency of the microwave radiation is swept, and the changes in the spin state of the center due to the interaction with external stimuli is detected by the optical technique. The operation of the hybrid system involves scanning a sample surface with the cantilever that houses the NV centers, enabling the measurement of multiple physical quantities, such as mechanical forces, magnetic, electronic, and thermal fields. This system finds applications in biological and chemical sensing, quantum sensing, and nanomechanics.

The characterization of various physical quantities based on the NV-cantilever beam is demonstrated in Figure 9. The sensitivity and spatial resolution of this system are dominated by the distance between the NV centers and the sample of interest, which usually is 50-100 nm. Figure 9(a), (b), and (c) show an illustration of magnetic measurement in the form of static, microwave and vortex fields, respectively. The characterization of the static magnetic field distribution of a commercial magnetic hard disk is achieved by measuring the difference of PL for two fixed MW frequencies, which are applied consecutively at each scan point. This method enhances the contrast of the dual iso-magnetic field image by suppressing background luminescence from the sample. The area with magnetic materials located or not are distinctly shown in Figure 9(a). When the scanning probe containing the NV centers is scanned at a height over the current stripline, the magnetic field generated by the current passing through the stripline could be detected by the NV magnetometer [173]. In Figure 9(b), isofield imaging of a MW magnetic field generated by high frequency (GHz) MW current is demonstrated. The method enables nanoscale resolution and three-dimensional reconstructing for imaging of MW magnetic field, thereby determining the local MW current density. As for the magnetic vortex generated by the small size (≈ 10 nm) of the vortex core, the scanning nitrogen-vacancy magnetometer also possesses the ability to image

it [172]. Figure 9(c) depicts an AFM image of a square of $Fe_{20}Ni_{80}$ with a thickness of 50 nm and a 5 μm side length, which reveals the distribution and the direction of the magnetic vortex. It is expected the scanning NV magnetometry may detect exotic magnetic structures such as skyrmion lattices.

The Zeeman splitting of the spin level of the NV center will occur when a magnetic field is applied. This distinguished splitting provides the ultra-high magnetic field resolution, which can be used to determine the magnetic gradient and therefore to measure displacement. An example of displacement measurement is shown in Figure 9(d), which demonstrates the Zeeman splitting frequency of the ESR fluorescence signal is linearly with the displacement [174]. By monitoring the quantum decoherence of an NV probe in proximity to the ion channel, lipid bilayer, or surrounding aqueous environment, the cell membrane ion-channel operation can be real-time detected at millisecond resolution. Figure 9(e) shows the ion-channel operation changes over time. The NV-based scanning method has the potential to revolutionize the characterization of the action of ion channels and other membrane proteins, with significant implications for molecular biology and drug discovery. Due to the asymmetry of the molecular orbits, as shown in Figure 7(b), the electric dipole moment will be generated and then the electron level of the NV center will shifted via the Stark effect when an electric field is applied. By monitoring the changes in NV fluorescence spectroscopy spectra when the scanning NV electrometry is swept along the surface, the alternating (AC) and direct (DC) electric fields of the sample can be imaged. Figure 9(f) provides a 2D map of the AC electric field in a U-shaped Au structure, indicating that the scanning NV electrometry achieves AC E-field sensitivity of 26 mV μm^{-1} $Hz^{-1/2}$ and DC E-field gradient sensitivity of 2 V μm^{-1} $Hz^{-1/2}$ [175]. The NV center in diamond offers numerous advantages, such as photostability, nonblinking behavior, and stable florescence, making it a stable emitter for the near field microscopy applications. By mounting the nanodiamonds with single NV centers on the tip of an AFM, the short-range fluorescence resonance energy transfer (FRET) between a donor and an acceptor will be detected optically. A three-dimensional image can be reconstructed by correlating the emission time of the recorded fluorescence photons with the phase of the oscillating cantilever [176]. Figure 9(g) illustrates the near-field images of graphene mono- and multiple layers obtained throught this technique. This approach is expected to further facilitate the development of multifunctional scanning microscopes that incorporate NV centers with cantilevers. The utilization of this technique will likely lead to promising applications in numerous fields such as the excitation-photonic nanostructures or single-fluorescence molecular imaging. Additionally, this method enables imaging of energy transfer into arbitrary nanostructures, mapping changes in material properties, and injecting single plasmons in various materials instead of excitons. The scanning FRET technique could also be an advantageous addition to other FRET-based techniques, especially for imaging larger protein structures of cellular surfaces. The combination of these methods with the magnetic field sensing capabilities of the NV center could potentially result in a truly multifunctional and highly versatile local probe.

7 Spin-strain coupling in diamond MEMS device

The mechanical strain provides another degree of freedom to modulate the spin state of the NV center. By embedding NV centers in diamond nanomechanical resonator, the energy structure of the NV centers could be mediated by strain modulation with the different mechanical amplitudes and resonant modes. The spin-strain interaction in the NV center arise from the coupling between the center's electronic spin and the local strain field that is caused by the deflection in the diamond lattice. This interaction bears similar to the spin-electric coupling, as both are caused by the variation of electric field. Compared to photons, phonons have more slower velocities, which results in looser timing requirements for chips. Moreover, phonons are unable to propagate in vacuum, enabling the creation of low-loss systems with mechanical oscillations that are highly isolated as opposed to optical systems. This feature offers the potential for long-range coherent interactions between qubits mediated by phonon modes instead of optical or microwave modes. It displays potential applications in the field of quantum metrology, quantum computing, quantum identifying, and mechanical quantum state [177].

If the NV center in diamond experiences magnetic or strain fields, the degeneracy of $|\pm 1\rangle$ will be lifted and the spin Hamiltonian takes the form ($h = 1$) [178, 179]:

$$H = D_0 S_z^2 + \gamma_{\mathrm{NV}} \vec{S} \cdot \vec{B} + d_{\parallel} \epsilon_z S_z^2 - d_{\perp}/2[\epsilon_+ S_+^2 - \epsilon_- S_z^2] \tag{13}$$

Here $\gamma_{\mathrm{NV}} = 2.799$ MHz/G, $\vec{B}$, and $\vec{S}$ are the NV gyromagnetic ratio, the external magnetic field, and the NV spin operator with $S_{\pm} = S_x \pm S_y$, respectively. $d_{\parallel}$ and $d_{\perp}$ are the strain susceptibility parameters parallel and perpendicular to the NV symmetry axis.

The characterization of the coupling between a mechanical resonator and an embedded single spin through lattice strain is crucial for the development of applications involving these system. In a study by Maletinsky et al., single-crystal diamond cantilevers with embedded NV center spins were used for the first time to determine the spin-strain coupling constants and demonstrate that this system resides well within the resolved sideband regime [180]. The fundamental flexural mode of one diamond cantilever had the resonance frequency as $\omega_{\mathrm{mech}} = 2\pi \times 6.695$ MHz with a linewidth of $\Delta\omega_{\mathrm{mech}} = 2\pi \times 28.7$ kHz, and the Q factor was estimated to be $Q = \omega_{\mathrm{mech}}/\Delta\omega_{\mathrm{mech}} = 232$. The confocal image of some cantilever devices with embedded NV center is shown in Figure 10(a), which shows individual, implanted NV centers scattered across the sample surface. The strain coupling constants corresponding to strain longitudinal $d_{\parallel}$ and transverse $d_{\perp}$ to the NV axis are determined via the optically detected electron spin resonance (ESR) of an NV center in the cantilever, in which the variable degree of strain experienced by the NV center near the clamping point of the cantilevers are achieved by the controlled cantilever bending. The strain coupling constants were determined by fitting the experimental ESR line, giving $d_{\parallel} = 5.46 \pm 0.31$ GHz per strain and $d_{\perp} = 19.63 \pm 0.40$ GHz per strain. The strain splitting of NV ESR lines as a function of static cantilever displacement is shown in the bottom panel of Figure 10(a).

The spin-strain coupling between the mechanical motion and the spin of embedded NV center could also be characterized by detecting the spin-dependent fluorescence through coherent quantum control of the spin [181]. As for the structure of the NV centers embedded in a diamond cantilever, the strain susceptibility parameters in parallel and perpendicular to the NV symmetry axis are determined as $d_{\parallel} = 13.3 \pm 1.1$ GHz per strain and $d_{\perp} = 21.5 \pm 1.2$ GHz per strain via this method [28]. The discrepancy between these two works is attributed to the difference in the detection technique and the mechanical resonant modes that were involved. Figure 10(b) shows the distribution of the NV centres in the diamond cantilever and the dependence of axial strain coupling strength on the distance from the clamping base. It is revealed that the coupling strength between the mechanical strain and the NV ground state decreases with increasing distance of the NV centers from the base, suggesting that the strains near the base are larger than those at other positions. In another study, shifts of the NV ground-state crystal field splitting were measured under hydrostatic pressure, and a strain coupling constant of $d_{\parallel} = 17.5$ GHz per strain was obtained [182].

By utilizing the coupling between strain in nanodiamonds and the spin degrees of freedom of the NV centers, it is possible to encode large variances of axial and transverse strains in nanodiamond clusters into a single radio frequency signature. Figure 10(c) demonstrates a diamond lattice and the direction of the strain field along (axial) the NV axis and perpendicular (transverse) to it (top). The bottom displays the transverse strain map of a collection of nanodiamonds dispersed on a glass substrate and the machine-readable QR code that includes the strain distribution of each NV centers, respectively [183]. This approach has the potential to make nanodiamond clusters highly useful for applications in anti-counterfeiting and biological tracking.

The modulation of the strain in diamond nanobeam can be used to generate effective spin-spin interaction between NV centers. By utilizing the spin echo techniques and mechanical driving, spin dephasing and mechanical dissipation could be suppressed while preserving the coherent spin-spin interactions, offering the possibility to generate squeezed states of a spin ensemble. Figure 10(d) displays a doubly clamped mechanical resonator with an ensemble of embedded NV centers (top) and the corresponding squeezing of the spin uncertainty distribution. This opens the possibility for long range coherent interac-

tions between qubits which are mediated by phonon modes instead of optical or MW ones [184].

In addition to the strain from the flexural modes, that from the bulk acoustic mode or surface acoustic mode can also couple the NV center spins and facilitate specialized control and manipulation. Bulk acoustic mode (BAM) is the collective motion of atoms in a material, which can be excited by an external mechanical perturbation. A bulk acoustic resonator can be fabricated by depositing a thin film of piezoelectric material, such as ZnO and AlN, on a substrate and then sandwiching the material with metal electrodes. When a voltage is applied to the metal electrodes, an electric field is induced in the piezoelectric film, causing it to vibrate at a resonant frequency. The coupling between the NV centers and the strain generated from the bulk acoustic mode has been reported [185, 186, 187, 188]. The acoustic modes allow mechanical manipulation of deeply embedded NV centers with long spin and orbital coherence times. Based on the fact that the NV center density is not expected to affect the excited state coherence time, Fuchs et al. demonstrated that a mechanical resonator could be cooled from room temperature to a fraction of its thermal phonon occupancy via the spin-strain coupling between the mechanical strain and excited state [185]. Figure 10(e) displays the schematic of the device (top) and the relationship between the NV density and final phonon numbers (bottom). Moreover, the interaction between the NV spin and mechanical strain has been successfully demonstrated in the surface acoustic mode [189, 190, 191]. Wang et al. reported that the coupling between the excited state and the strain through a Λ-type three-level system, in which two ground spin states couple to a common excited state through a phonon-assisted and the direct dipole optical transition [192]. Coherent manipulation between the phonon and spin in diamond provides an experimental platform for spin-based quantum acoustics, bridging the gap between spintronics and quantum acoustics.

The interaction of solid-state electronic spins with the deformations of their host crystal is an important ingredient in many experiments aimed at realizing quantum information processing schemes. The importance of this interaction is evidenced by the ability to be actuated mechanically or electrically to achieve spin transition that are controlled by magnetic field in current experiments, as well as the spin transition that cannot be achieved experimentally with magnetic field. By replacing magnetic field drive with AC strain or AC electric field, this method offers considerable benefits for device miniaturization, reduced power requirements, and local addressability of electronic spin qubits [29]. By enhancing the coupling between the mechanical strain and spin of the NV center in diamond [193], a number of applications such as stress characterazation[194], creation of squeeze mechanical states [195], cooling of a mechanical resonator to its ground state [177, 185, 196, 197] and spin-phonon entanglement [198] can be achieved.

8 Cavity optomechanics based on diamond mechanical resonators

The cavity optomechanics study the interaction between the cavity photons and the moving mechanical oscillation. The origin of the research field *cavity optomechanics* is closely related to the development of gravitational wave detection using laser interferometer, e.g., LIGO. The concept of optomechanical interaction is built up to answer the question of how the mirror zero-point fluctuation and cavity field shot-noise block the detection of gravitation wave. Meanwhile, Thorne et al. conceived the idea of quantum backaction evasion measurement [199]. Benefitted from the modern advanced micro/nano fabrication technology, versatile cavity optomechanical devices are mushrooming and booming up [200]. Intriguing phenomena including optomechanical induced, e.g., transparency [201], absorption [202, 203], chaos [204], synchronization [205], and phonon lasing [206] were demonstrated based on the radiation pressure interaction. In addition to exploring the above classical phenomena, the studies of cavity optomechanics have entered into the quantum regime. On one hand, the cavity optomechanical system itself is a precise measurement setup. Mason et al realized continuous force and displacement measurements below the standard quantum limit [207]. Prudy et al. observed the radiation pressure shot noise on a macroscopic object [208]. On the other hand, cavity optomechanical systems are becoming powerful platform to study the fundamental debate about quantum mechanics, such as the classical gravity effects on the quantum state decoherence [209]. In any case, the prerequisite for conducting research at the

quantum level is to reduce the thermal noise of the mechanical oscillator, that is, to realize the ground state cooling of the macroscopic mechanical oscillator.

The ability to cool the mechanical resonators to the ground-state through the interaction with photons has sparked an explosion of interest in the study of fundamental physics and also paves the way to the building up of a veritable quantum toolbox [210, 211, 212]. The motional quadrature fluctuation could be squeezed below the zero-point level with combined blue- and red-detuned driving tones [213, 214, 215]. Inseparable from parametric squeezing, nonclassical correlations between the mechanical motion and the cavity field [216, 217, 218], entanglement generation of microwave radiation [219], and non-classical state shared between two mechanical oscillators [220, 221] have been realized in experiments. Correlation function [222], optomechanical Bell inequality [223] and backaction-evasion [224, 225] measurements demonstrated a significant improvement in the ability to directly readout and manipulate the quantum states of mechanical oscillators, which could be viewed as the start point of exploring long-sought-after theory, e.g., collapse models [226] and gravitational dechoerence [227, 228, 209, 229].

Along with the great achievements made in fundamental exploration, optomechanical systems present unique advantages and show fascinating applications in emerging quantum technologies [230]. The capability of wavelength conversion plays a special role in quantum networks. The mechanical resonators can couple with any of the optical resonances and then convert the quantum information from a given wavelength to the other which can couple to another quantum system. Moreover, the mechanical resonator whose functionality is flexibly designed can be directly coupled to various natural or artificial quantum systems, thus, constituting ideal tools for quantum transducers and interfaces. In particular, using optomechanical transducer, electrical quantum processors can be connected to optical photons that is suitable for long distance telecommunication [231].

Gigahertz mechanical resonators can be passively cooled into their ground-state in a dilution refrigerator, and they can be used to couple directly to microwave qubits through the piezoelectric effect [211, 210]. The bidirectional electro-optical conversion through piezoelectric resonators had been successfully demonstrated [232, 233, 234]. Meanwhile, kilohertz or megahertz mechanical resonators parametrically coupled to optical or microwave cavities, has the advantage of, e.g., not requiring frequency matching, achieving near-unit efficiency, and low-noise operation of a superconducting qubit. A major impediment is the added noise raised by thermal occupation of mechanical modes. High Q factors have made these low-frequency mechanical resonators more accessible to reach their quantum ground-state with sideband cooling techniques [200]. Usually the electro-optical conversion is a continuous process. For example, microwave photons are coherently down-converted to mechanical oscillators, simultaneously, they are parametrically up-converted to photons with an additional laser pumping. It is notable that the transduction process is reciprocal and the long-lived phonons play a key intermediary role. The microwave or optical quantum state could be coherently transferred inside the mechanical resonators, demonstrating another intriguing capability to use long-lived phononic modes for quantum memories and repeaters.

Cavity optomechanical systems usually involve the interaction between the cavity field and mechanical resonators through two mechanisms: moving mechanical boundaries and photoelasticity. The mechanical displacement of the movable cavity walls is a boundary effect, while the photoelastic scattering is a bulk response, manifested as a modulation of the refractive index of the cavity material by strain. The single-photon optomechanical coupling strength parameter g_0 is used to quantify the light-matter interaction. Here, g_0 is calculated as the product of the optical frequency shift per unit displacement and the amplitude of the zero-point fluctuations of the corresponding mechanical oscillator modes. In the designed stage, the parameter of optical-mechanical coupling strength can be simulated and optimized by using perturbation theory and finite element numerical simulation. Experimentally, this parameter can be obtained by fitting the optical spring effect and optomechanical damping. In order to realize the application in the quantum field, the optomechanical cooperative coupling parameter $C_{\rm om}$ must be strong enough: $C_{\rm om} = 4n_c g_0^2/\kappa\gamma_m > 1$. Here, κ and γ_m correspond to the energy decay rates of the cavity field and mechanical modes, respectively, and n_c is the average number of photons in the cavity. The $C_{\rm om} > 1$

condition has been achieved in various cavity optomechanical systems, including those made of diamond. The Hamiltonian describing the optomechanical system is given as follows:

$$H_{CM} = \hbar\omega_a a^\dagger a + \hbar\omega_m m^\dagger m + \hbar g(a^\dagger + a)(m + m^\dagger), \tag{14}$$

Where, $a^\dagger$ (a) and $m^\dagger$ (m) are the creation (annihilation) operators for the cavity field and mechanical mode, respectively. ω_a and ω_m are the resonance frequency of optical cavity and mechanical resonator, respectively. The expansion of the final term in Equation (14) yields the Jaynes-Cummings-like interaction terms $\hbar g(a^\dagger m + a m^\dagger)$ and the term of $\hbar g(a^\dagger m^\dagger + a m)$, which arises from the inherent nonlinearity of optomechanical interaction and is the resource of the squeezing and entanglement. It is notable that the optomechanical coupling has been linearized and the Hamiltonian in Equation (14) is in an rotating coordinate frame with driving frequency ω_d. Generating quantum state transfer between photons and phonons requires the condition $C_{\mathrm{om}} > n_{th} + 1$, where n_{th} is the average number of thermal phonons generated by coupling to its thermal bath. To lower n_{th}, either cooling the resonator to cryogenic temperatures, or using a high frequency resonator, sometimes a combination of both are employed. Another key parameter is the sideband resolution region, that is, the mechanical mode frequency of the resonator exceeds κ, it can be used for quantum limited amplification of optical field with blue-detuned driving or to realize the mechanical sideband cooling with red-sideband driving. In the above discussion, we only considered the real part of the optomechanical interaction g_0. If the mechanical displacement causes a significant change in the optical loss of the cavity, g_0 will be complex. In this case, the system holds both the dispersion and dissipative coupling terms.

Cavity optomechanical systems based on single-crystal diamond materials are expected to benefit from their extraordinary material properties, including the highest Young's modulus, low mechanical dissipation and wide optically transparent windows. Here, we introduce the recent development of cavity optomechanical devices based on the diamond mechanical resonators for tuning and controlling the color centers and their potential applications as quantum memory and quantum interface. Khanaliloo et al. creatively cut a cantilever beam, as shown in Figure 11(a), from a bulk SCD substrate, and then dissipatively coupled and readout the mechanical oscillator through an optical fiber [235]. The nanomechanical oscillator was evanescently coupled to the fiber tapered waveguide and excited to self-excited oscillation by the optical field through the optomechanical coupling. The mechanical oscillator amplitude was larger than 200 nm when the incident power was 100 nW, implying an internal stress of 70 MPa in the diamond cantilever. The dissipative optical mechanical coupling strength was up to 45 GHz/nm (0.48 MHz per photon), and the displacement sensitivity was 9.5 fm/$\sqrt{\mathrm{Hz}}$. The resonance frequency of the typical nanobeam waveguide was around 1.58 MHz, and the Q factor of the mechanical mode reached ($Q_m > 7.2 \times 10^5$). Later, Harishankar, et al., demonstrated tunable amplification and damping of the mechanical oscillation of a diamond nanomechanical resonator using a confocal microscope [236]. The mechanical mode was cooled from room temperature to 80 K via waveguide optomechanical interaction.

Matthew and coauthors demonstrated a SCD microdisk cavity optomechanical device that could realize photon-phonon coupling [237]. The device parameters were characterized by monitoring the optical field transmission characteristics within the fiber cone coupled with the microdisk. Experimentally, the input laser detection length comes from a tunable diode laser at 1530 or 637 nm. Under room temperature ambient conditions, the mechanical vibration frequency was up to 2 GHz, the quality factor reached $Q_m > 9\,000$, and $Q_m \times f_m = 1.9 \times 10^{13}$. These parameters indicate that the device is capable of single-phonon coherent manipulation at room temperature. Its mechanical self-oscillation with an amplitude of 31 pm is expected to provide a coupling rate of 0.6 MHz for the ground-state transition (6 Hz/phonon) of the diamond NV center. This experiment demonstrates the potential of photodynamic radiation pressure to coherently control diamond electron spins. Multiple optical modes exist in such diamond microdisk cavity, as shown in Figure 11(b). Radiation pressure was exerted by optical whispering gallery modes on the microdisk produces optomechanical coupling. When the two optical modes of the microdisk are coupled to the common mechanical mode at the same time, the energy transfer between different optical modes can be realized by controlling the optical mechanical coupling parameters, that is, wavelength conversion. When the pump laser frequency is below (above) a mechanical res-

onance frequency of the optical resonance mode, we call it red (blue) sideband driving. Optomechanical coupling driven by red sidebands is a beam splitter-type interaction that coherently exchanges energy between the optical cavity field and the mechanical domain. Mitchell et al. demonstrated mechanic-induced wavelength conversion on a microdisk [238] made of single-crystal diamond with an internal efficiency of about 45%, and this work simultaneously demonstrated optomechanical frequency conversion with amplification in the optical range.

The construction of quantum Internet often requires the efficient switching and routing of photons of different wavelengths. Multimode optomechanical systems are one of the hot candidates to address this technical challenge. To this end, Lake, et al., demonstrated two photomechanically induced transparency processes on diamond microdisks and systematically studied their mutual competition and interference [239]. The simultaneous action of different cavity fields on the same mechanical mode will induce the optomechanical dark mode. Such dark modes do not transfer energy to dissipative mechanical oscillators, and thus can be used to realize quantum information transmission applications that are insensitive to mechanical decoherence. Experimentally, by adjusting the phase difference between the detection fields of different wavelengths incident into the cavity, the controllable excitation of the mechanical bright mode or the mechanical dark mode can be realized. This work further demonstrates the controllable coupling between the two modes. Subsequently, Lake et al. demonstrated real-time controlled optical information storage in a diamond microdisk cavity optomechanical system. Further driving through the blue sideband breaks through storage lifetime limited by the inherent damping of the mechanical mode [240].

Burek et al. fabricated optomechanical crystals (OMCs) on bulk diamond material by angle etching [241]. The final fabricated device is illustrated in Figure 11(c). The authors employed anisotropic oxygen-based plasma etching at an oblique angle to the substrate surface, resulting in suspended structures with a triangular cross-section as disclosed by the SEM image. The diamond nano-optomechanical device is quasi-periodic, providing an optical resonance mode around 200 THz and mechanical vibration modes at frequencies of 5.5 and 9.5 GHz. The local phonons changed the effective refractive index and other parameters of the material photoelasticity, causing the dispersion shift of the frequency of the photonic crystal resonator and leading to dispersion-optomechanical coupling in the form of optomechanical radiation pressure. The vacuum optomechanical coupling rates were given as $g_a/2\pi \sim 120$, and $g_b/2\pi \sim 220$ kHz, respectively. The diamond OMC device was measured with an optical linewidth of $\kappa/2\pi \sim 1.1$ GHz, operating in the so-called sideband-resolved regime ($\omega_m/\kappa > 1$), which is important for realizing the sideband cooling of the mechanical oscillator based on the dynamic backaction of the cavity field under the radiation pressure. Compared to other materials, the photonic crystal microcavity made of diamond accommodates more than 10^5 photons without obvious nonlinearity. Based on a sufficient number of photons in the cavity, the diamond OMC has a sufficiently high optomechanical coupling strength at room temperature, and the optomechanical cooperativity reaches $C_{\mathrm{om}} \sim 20$, allowing further observations of optomechanically induced transparency and the realization of large-amplitude optomechanical self-excited oscillations.

Strain in the lattice of diamond single crystal materials can induce the coherent coupling of NV electron spins with quantized mechanical vibrations (phonons). The prediction and observation of spin-phonon coupling have promoted the application and development of diamond nanomechanical devices in the direction of hybrid quantum systems. When the cavity-field radiation pressure interaction is introduced, the coherent phonons of the diamond mechanical oscillator provide a quantum coherent interface for solid-state spin storage of optical information. Prasoon et al. demonstrated a new method to control the electron spin of NV center based on cavity optomechanical interaction [242]. The experiment employed 5.3 μm diameter microdisks, produced mainly by isotropic plasma etching, on a diamond substrate (Element Six, optical grade) and intended to minimize the mechanical mode volume while possessing low optical microcavity dissipation. An optical cavity field mode with a wavelength $\lambda_c = 1564$ nm has a quality factor of $Q_c = 1.1 \times 10^5$. This optical mode was used to measure and drive the microdisk mechanical radial breathing mode. The displacement and stress distributions for this mode are shown in Figure 11(d).

The eigen frequency and quality factor of the mechanical radial breathing mode were $\omega_m/2\pi = 2.09$ GHz and $Q_m = 4\ 300$, respectively. The optomechanical coupling strength was $g_{om}/2\pi \approx 25$ kHz. A single phonon is expected to generate a stress of $P_0 \approx 1$ kPa, with stress concentrated in the microdisk's center. Although this value is close to the state-of-the-art, it is still too weak for single-phonon manipulation of NV ground-state spin qubits. In this work, the authors used a phonon laser methold to generate large mechanically coherent phonon states to enhance the coupling between phonons to NV center spins. The spin-optomechanical interface offers protection from spectral diffusion and allows for operation at telecommunication wavelengths with qubits lacking optical transitions. It is an important step towards universal coupling of telecom photons to hybrid quantum nodes built on spins and superconducting qubits.

Replacing the microdisk with an optomechanical crystal will further increase spin-mechanical coupling strength by three orders of magnitude and the use of phononic shield can improve both optomechanical coupling and spin-mechanical coupling strength. Toward reaching the quantum regime with spin qubit-mechanic hybrid devices, Jeffrey et al. demonstrated the fabrication of diamond optomechanical crystals (OMCs) with embedded NV centers, which host optical modes with quality factors of 42,000 and an acoustic breathing mode frequency near 6 GHz with a quality factors of 100 in ambient conditions [243]. The fabrication process preserves the long spin coherence time of $T_2 = 72$ μs. In order to further reduce the phonon thermal noise of photoacoustic crystals, which will be applied to coherent interfaces in future quantum networks, the characterization of the excited states of NV center at low temperature is needed. This is a crucial step towards reaching the quantum regime with spin-mechanic hybrid devices.

9 Conclusions and perspective

Diamond is emerging as an ideal and unique material for MEMS/NEMS either from the viewpoint of classic applications as those of Si MEMS or quantum science and technology. The outstanding mechanical strength, ultra-wide bandgap energy, and the highest thermal conductivity enable the construction of low-energy loss or high-quality-factor MEMS/NEMS resonators. PCD/NCD/UNCD has the advantages of large wafer size, low cost, and ability to grown on Si substrates, on which the Si micromachining process can be adopted. The fabrication of SCD MEMS, especially the smart-cut method, has been well established. MEMS devices made from diamond can endure harsh environments such as high temperature and strong radiation. High-temperature diamond MEMS sensors were demonstrated to be operable up to 500 °C. The applications of diamond MEMS has been steadily explored ranging from pressure sensors, mass sensors, RF switch, and magnetic fields.

The NV center in diamond is unique with a long coherence time and the ability to be optically initialized and read out. By integrating the nanodiamond with embedded NV centers onto an AFM cantilever resonator, the created hybrid system is compatible with scanning spatial resolution of the AFM probe and the sensitivities of NV centers. This system shows potential for application in characterizing the materials in the surface or the interior, enabling an ultra-sensitive detection of magnetic fields, electric fields, temperature, displacements, and biotracking. This coupling of strain by diamond MEMS with and quantum centers enables a host of applications in various fields, such as the strain detection of materials, quantum metrology, quantum computing, and cooling the diamond micro/nano mechanical resonator.

An optomechanical system comprising a cavity and diamond MEMS resonator can enhance and confine the magnetic and electric fields. This system provides a method of backaction cooling for the mechanical resonator to its quantum ground state, where the long lifetime phonon can be harnessed to store and process quantum information. Moreover, integrating NV centers with diamond optomechanical resonator would expand the functionality and leverage the individual advantages of each system. The optomechanical system has the potential to enable high-precision sensing and measurement of mechanical vibrations and optical transitions. It can also be used for quantum information processing applications, such as quantum sensing, quantum computing, and quantum communication.

Based on MEMS resonators, it is possible to completely replace the ac magnetic field with ac mechanical driving for spin control in NV quantum states. Various physical systems can naturally couple to the phonon system, such as solid state defect in a crystal, superconducting qubits, and atoms. Phonons are becoming a promising and flexible platform for coherently interfacing systems of disparate energy or different physical control mechanisms and can serve as a bus for the coherent information propagation of individual quantum nodes of module quantum computers.

In the future, efforts will be focused on improving the crystal quality of diamonds and the electrically integrated fabrication technologies of diamond MEMS resonators. These involve reducing the density of dislocation defects, developing new etch methods of diamond, and on-chip integration of diamond MEMS for either classic sensing or quantum technology. To obtain high quality-factor diamond MEMS resonators in for mass applications, the growth of large-size SCD wafer with high-crystal quality and reduction of energy dissipation from the surface and internals will be explored. Moreover, by introducing dissipation dilution through stress engineering on the structure design of MEMS resonators, the Q factors of diamond MEMS resonators can be further enhanced, thus, enabling SCD MEMS resonators for high-performance classic sensors and mechanical quantum state preparation. An advanced approach to improve the Q factor of MEMS/NEMS resonators is to introduce the well-known dissipation dilution mechanism. The core idea of dissipation dilution is to mitigate the energy dissipation originating from the clamped positions, which is always the predominant dissipative source of mechanical energy. This is generally accomplished by the sophisticated geometric design of the resonator, such as the phononic and fractal shape [244, 245, 246], in which the concerned mechanical resonant modes will be located within the band gap of generated from the period structure of the phononic crystal. The underlying causes of dissipation dilution can be attributed to the presence of tension and the geometrical nonlinearity arising from dynamic strain. This nonlinearity emerges as a result of the nonlinear stress-strain relationship and cannot be negligible even in the case of infinitesimal vibrations [247]. By introducing the phononic shield effect, Wang et al. successfully fabricated nanometer-scale diamond mechanical resonators, employing the cuboid cell architecture, with a quality factor exceeding 10^6 and $f \times Q > 10^{14}$ [248]. The phononic shields enable the development of high sensitivity and low noise classic and quantum devices.

Supporting Information

Supporting Information is available from the Wiley Online Library or from the author.

Acknowledgements

H.S and Z.Z contributed equally to this work. The authors gratefully acknowledge the support from Beijing Municipal Science and Technology Commission (Grant No. Z221100002722011), the Grant-in-Aid for JSPS Research Fellows (Grant No. 22F21341), JSPS KAKENHI (Grant No. 20H02212, 22K18957, 15H03999), Tsukuba Global Innovation Promotion Agency and Nanotechnology Platform projects sponsored by the Ministry of Education, Culture, Sports, and Technology (MEXT) of Japan, National Key Research and Development Program of China (Grant No. 2022YFA1405200) and the National Natural Science Foundation of China (Grants No. 12004044, and No. 62074091).

Conflict of Interest

The authors declare no conflict of interest.

References

[1] M. F. Bocko, R. Onofrio, *Rev. Mod. Phys.* **1996**, *68* 755.

[2] G. Gruber, C. Urgell, A. Tavernarakis, A. Stavrinadis, S. Tepsic, C. Magén, S. Sangiao, J. M. de Teresa, P. Verlot, A. Bachtold, *Nano Letters* **2019**, *19*, 10 6987, pMID: 31478676.

[3] D. Rugar, R. Budakian, H. J. Mamin, B. W. Chui, *Nature* **2004**, *430* 329.

[4] A. Ahmed, J. V. Rushworth, N. A. Hirst, P. A. Millner, *Clinical Microbiology Reviews* **2014**, *27*, 3 631.

[5] V. Puller, B. Lounis, F. Pistolesi, *Phys. Rev. Lett.* **2013**, *110* 125501.

[6] A. Uranga, J. Verd, N. Barniol, *Microelectronic Engineering* **2015**, *132* 58, micro and Nanofabrication Breakthroughs for Electronics, MEMS and Life Sciences.

[7] G. Pillai, S.-S. Li, *IEEE Sensors Journal* **2021**, *21*, 11 12589.

[8] R. W. Peterson, T. P. Purdy, N. S. Kampel, R. W. Andrews, P.-L. Yu, K. W. Lehnert, C. A. Regal, *Phys. Rev. Lett.* **2016**, *116* 063601.

[9] M. Rossi, D. Mason, J. Chen, Y. Tsaturyan, A. Schliesser, *Nature* **2018**, *563*, 7729 53.

[10] N. Yang, S. Yu, J. V. Macpherson, Y. Einaga, H. Zhao, G. Zhao, G. M. Swain, X. Jiang, *Chem. Soc. Rev.* **2019**, *48* 157.

[11] C. E. Nebel, *Functional Diamond* **2023**, *3*, 1 2201592.

[12] Z. Zhang, G. Chen, K. Gu, S. Koizumi, M. Liao, *Functional Diamond* **2023**, *3*, 1 2221280.

[13] Z. Zhang, H. Wu, L. Sang, Y. Takahashi, J. Huang, L. Wang, M. Toda, I. M. Akita, Y. Koide, S. Koizumi, M. Liao, *ACS Applied Materials & Interfaces* **2020**, *12*, 20 23155, pMID: 32336083.

[14] M. Liao, S. Hishita, E. Watanabe, S. Koizumi, Y. Koide, *Advanced Materials* **2010**, *22*, 47 5393.

[15] J. Webster, C. Dyck, J. Sullivan, T. Friedmann, A. Carton, *Electronics Letters* **2004**, *40*, 1 43.

[16] M. Liao, L. Sang, T. Teraji, S. Koizumi, Y. Koide, *Advanced Materials Technologies* **2019**, *4*, 2 1800325.

[17] S. Fujii, C. Jian, *IEEE Transactions on Ultrasonics, Ferroelectrics, and Frequency Control* **2012**, *59*, 12 2758.

[18] M. Oudich, M. Badreddine Assouar, *Journal of Applied Physics* **2012**, *111*, 1, 014504.

[19] K. O. Ho, Y. Shen, Y. Y. Pang, W. K. Leung, N. Zhao, S. Yang, *Functional Diamond* **2021**, *1*, 1 160.

[20] D. A. Golter, K. N. Dinyari, H. Wang, *Phys. Rev. A* **2013**, *87* 035801.

[21] S. Dhomkar, J. Henshaw, H. Jayakumar, C. A. Meriles, *Science Advances* **2016**, *2*, 10 e1600911.

[22] L. Rondin, J.-P. Tetienne, T. Hingant, J.-F. Roch, P. Maletinsky, V. Jacques, *Reports on Progress in Physics* **2014**, *77*, 5 056503.

[23] V. M. Acosta, E. Bauch, A. Jarmola, L. J. Zipp, M. P. Ledbetter, D. Budker, *Applied Physics Letters* **2010**, *97*, 17, 174104.

[24] Y. Dong, J.-Y. Xu, S.-C. Zhang, Y. Zheng, X.-D. Chen, W. Zhu, G.-Z. Wang, G.-C. Guo, F.-W. Sun, *Functional Diamond* **2021**, *1*, 1 125.

[25] R. Schirhagl, K. Chang, M. Loretz, C. L. Degen, *Annual Review of Physical Chemistry* **2014**, *65*, 1 83.

[26] C. Ju, C. Lei, X. Xu, D. Culcer, Z. Zhang, J. Du, *Phys. Rev. B* **2014**, *89* 045432.

[27] E. Togan, Y. Chu, A. S. Trifonov, L. Jiang, J. Maze, L. Childress, M. V. G. Dutt, A. S. Sørensen, P. R. Hemmer, A. S. Zibrov, M. D. Lukin, *Nature* **2010**, *466*, 7307 730.

[28] P. Ovartchaiyapong, K. W. Lee, B. A. Myers, A. C. B. Jayich, *Nature Communications* **2014**, *5* 4429.

[29] A. Barfuss, M. Kasperczyk, J. Kölbl, P. Maletinsky, *Phys. Rev. B* **2019**, *99* 174102.

[30] S. Imanishi, K. Kudara, H. Ishiwata, K. Horikawa, S. Amano, M. Iwataki, A. Morishita, A. Hiraiwa, H. Kawarada, *IEEE Electron Device Letters* **2021**, *42*, 2 204.

[31] M. Kianinia, I. Aharonovich, *Nature Photonics* **2020**, *14*, 10 599.

[32] C. Yu, C. Zhou, J. Guo, Z. He, M. Ma, H. Yu, X. Song, A. Bu, Z. Feng, *Functional Diamond* **2022**, *2*, 1 64.

[33] Z. Zhang, L. Sang, J. Huang, W. Chen, L. Wang, Y. Takahashi, S. Mitani, Y. Koide, S. Koizumi, M. Liao, *Carbon* **2020**, *170* 294.

[34] L. Sang, *Functional Diamond* **2021**, *1*, 1 174.

[35] J. Davidson, R. Ramesham, C. Ellis, *Journal of the Electrochemical Society* **1990**, *137*, 10 3206.

[36] E. Kohn, P. Gluche, M. Adamschik, *Diamond Related Materials* **1999**, *8*, 2-5 934.

[37] A. Krauss, O. Auciello, D. Gruen, A. Jayatissa, A. Sumant, J. Tucek, D. Mancini, N. Moldovan, A. Erdemir, D. Ersoy, *Diamond Related Materials* **2001**, *10*, 11 1952.

[38] J. E. Butler, A. Sumant, *Chemical Vapor Deposition* **2008**, *14*, 7-8 145.

[39] M. Liao, C. Li, S. Hishita, Y. Koide, *Journal of Micromechanics Microengineering* **2010**, *20*, 8 085002.

[40] S. D. Janssens, D. Vzquez-Corts, A. Giussani, J. A. Kwiecinski, E. Fried, *Diamond and Related Materials* **2019**, *98* 107511.

[41] O. Auciello, D. M. Aslam, *Journal of Materials Science* **2021**, *56*, 12 7171.

[42] V. Sedov, A. Martyanov, S. Savin, E. Zavedeev, O. Kudryavtsev, H. Bland, S. Mandal, O. Williams, V. Ralchenko, V. Konov, *Diamond and Related Materials* **2021**, *114* 108333.

[43] N. Sepúlveda, J. Lu, D. M. Aslam, J. P. Sullivan, *Journal of microelectromechanical systems* **2008**, *17*, 2 473.

[44] X. Zhu, D. M. Aslam, Y. Tang, B. H. Stark, K. Najafi, *Journal of Microelectromechanical Systems* **2004**, *13*, 3 396.

[45] N. Sepúlveda-Alancastro, D. M. Aslam, *Microelectronic engineering* **2004**, *73* 435.

[46] N. Sepúlveda, D. Aslam, J. P. Sullivan, *Diamond Related Materials* **2006**, *15*, 2-3 398.

[47] O. Auciello, J. Birrell, J. A. Carlisle, J. E. Gerbi, X. Xiao, B. Peng, H. D. Espinosa, *Journal of Physics: Condensed Matter* **2004**, *16*, 16 R539.

[48] L. Sekaric, J. M. Parpia, H. G. Craighead, T. Feygelson, B. H. Houston, J. E. Butler, *Applied Physics Letters* **2002**, *81*, 23 4455.

[49] A. V. Sumant, O. Auciello, R. W. Carpick, S. Srinivasan, J. E. Butler, *MRS bulletin* **2010**, *35*, 4 281.

[50] O. Williams, *Diamond and Related Materials* **2011**, *20*, 5 621 .

[51] J. W. Baldwin, M. Zalalutdinov, T. Feygelson, J. E. Butler, B. H. Houston, *Journal of Vacuum Science Technology B* **2006**, *24*, 1 50.

[52] J. W. Baldwin, M. K. Zalalutdinov, T. Feygelson, B. B. Pate, J. E. Butler, B. H. Houston, *Diamond Related Materials* **2006**, *15*, 11-12 2061.

[53] J. Fu, T. Zhu, Y. Liang, Z. Liu, R. Wang, X. Zhang, H.-X. Wang, *Scientific Reports* **2019**, *9*, 1 4699.

[54] M. Liao, Y. Koide, L. Sang, *Single Crystal Diamond Micromechanical and Nanomechanical Resonators*, 91–121, Springer, **2019**.

[55] L. B. Casabianca, A. I. Shames, A. M. Panich, O. Shenderova, L. Frydman, *The Journal of Physical Chemistry C* **2011**, *115*, 39 19041.

[56] S. Kolkowitz, A. C. Bleszynski Jayich, Q. P. Unterreithmeier, S. D. Bennett, P. Rabl, J. Harris, M. D. Lukin, *Science* **2012**, *335*, 6076 1603.

[57] I. Wilson-Rae, P. Zoller, A. Imamoğlu, *Physical Review Letters* **2004**, *92*, 7 075507.

[58] P. Olivero, S. Rubanov, P. Reichart, B. C. Gibson, S. T. Huntington, J. Rabeau, A. D. Greentree, J. Salzman, D. Moore, D. N. Jamieson, *Advanced Materials* **2005**, *17*, 20 2427.

[59] M. Liao, M. Toda, L. Sang, T. Teraji, M. Imura, Y. Koide, *Japanese Journal of Applied Physics* **2017**, *56*, 2 024101.

[60] P. Ovartchaiyapong, L. M. A. Pascal, B. A. Myers, P. Lauria, A. C. Bleszynski Jayich, *Applied Physics Letters* **2012**, *101*, 16 163505.

[61] Y. Tao, C. Degen, *Advanced Materials* **2013**, *25*, 29 3962.

[62] M. J. Burek, D. Ramos, P. Patel, I. W. Frank, M. Lončar, *Applied Physics Letters* **2013**, *103*, 13 131904.

[63] M. J. Burek, N. P. de Leon, B. J. Shields, B. J. M. Hausmann, Y. Chu, Q. Quan, A. S. Zibrov, H. Park, M. D. Lukin, M. Lončar, *Nano Letters* **2012**, *12*, 12 6084.

[64] M. Liao, *Functional Diamond* **2021**, *1*, 1 29.

[65] N. Parikh, J. Hunn, E. McGucken, M. Swanson, C. White, R. Rudder, D. Malta, J. Posthill, R. Markunas, *Applied Physics Letters* **1992**, *61*, 26 3124.

[66] Y. Tao, J. M. Boss, B. A. Moores, C. L. Degen, *Nature Communications* **2014**, *5* 3638.

[67] W.-M. Zhang, K.-M. Hu, Z.-K. Peng, G. Meng, *Sensors* **2015**, *15*, 10 26478.

[68] K. Eom, H. S. Park, D. S. Yoon, T. Kwon, *Physics Reports* **2011**, *503*, 4-5 115.

[69] W. Weaver Jr, S. P. Timoshenko, D. H. Young, *Vibration problems in engineering*, John Wiley & Sons, **1991**.

[70] M. Imboden, P. Mohanty, *Physics Reports* **2014**, *534*, 3 89 .

[71] H. Sun, L. Sang, H. Wu, Z. Zhang, T. Teraji, T.-F. Li, J. Q. You, M. Toda, S. Koizumi, M. Liao, *Physical Review Letters* **2020**, *125* 206802.

[72] H. Wu, L. Sang, T. Teraji, T. Li, K. Wu, M. Imura, J. You, Y. Koide, M. Liao, *Carbon* **2017**, *124* 281.

[73] J. Wang, J. E. Butler, D. Hsu, C. T.-C. Nguyen, *Tech. Digest* **2002**, 2–6.

[74] Y. Gurbuz, W. P. Kang, J. L. Davidson, D. V. Kerns, *Sensors Actuators B: Chemical* **2004**, *99*, 2-3 207.

[75] L. Saturday, L. Wilson, S. Retterer, N. J. Evans, D. Briggs, P. D. Rack, N. Lavrik, *Diamond Related Materials* **2021**, *113* 108279.

[76] D. Saito, C. Yang, A. Heidari, H. Najar, L. Lin, D. A. Horsley, In *2015 28th IEEE International Conference on Micro Electro Mechanical Systems (MEMS)*. IEEE 801–804.

[77] R. Müller, P. Schmid, A. Munding, R. Gronmaier, E. Kohn, *Diamond Related Materials* **2004**, *13*, 4-8 780.

[78] S. Guillaudeu, X. Zhu, D. Aslam, *Diamond Related Materials* **2003**, *12*, 1 65.

[79] R. Ramesham, T. Roppel, C. Ellis, M. Rose, *Journal of the Electrochemical Society* **1991**, *138*, 6 1706.

[80] P. Rath, S. Khasminskaya, C. Nebel, C. Wild, W. H. Pernice, *Nature Communications* **2013**, *4*, 1 1690.

[81] J. Haas, E. V. Catalán, P. Piron, F. Nikolajeff, L. Österlund, M. Karlsson, B. Mizaikoff, *ACS Omega* **2018**, *3*, 6 6190.

[82] J. K. Luo, Y. Q. Fu, H. R. Le, J. A. Williams, S. M. Spearing, W. I. Milne, *Journal of Micromechanics and Microengineering* **2007**, *17*, 7 S147.

[83] E. Kohn, M. Adamschik, P. Schmid, S. Ertl, A. Fl?ter, *Diamond Related Materials* **2001**, *10*, 9-10 1684.

[84] J. Kusterer, P. Schmid, E. Kohn, *New Diamond and Frontier Carbon Technology* **2006**, *16*, 6 295.

[85] W. Kulisch, A. Malave, G. Lippold, W. Scholz, C. Mihalcea, E. Oesterschulze, *Diamond Related Materials* **1997**, *6*, 5-7 906.

[86] O. Auciello, S. Pacheco, A. V. Sumant, C. Gudeman, S. Sampath, A. Datta, R. W. Carpick, V. P. Adiga, P. Zurcher, Z. Ma, H. Yuan, J. A. Carlisle, B. Kabius, J. Hiller, S. Srinivasan, *IEEE Microwave Magazine* **2007**, *8*, 6 61.

[87] C. Wang, Y. Choi, J. Lee, E. Hu, J. Yang, J. Butler, *Applied Physics Letters* **2007**, *90*, 8 081110.

[88] K. Kim, N. Moldovan, C. Ke, H. D. Espinosa, X. Xiao, J. A. Carlisle, O. Auciello, *Small* **2005**, *1*, 8-9 866.

[89] J. Liu, D. S. Grierson, N. Moldovan, J. Notbohm, S. Li, P. Jaroenapibal, S. O'Connor, A. Sumant, N. Neelakantan, J. A. Carlisle, *Small* **2010**, *6*, 10 1140.

[90] S. P. Pacheco, P. Zurcher, S. R. Young, D. Weston, W. J. Dauksher, O. Auciello, J. A. Carlisle, N. Kane, J. P. Birrell, In *2005 European Microwave Conference*, volume 3. IEEE, **2005** 4–pp.

[91] A. Sumant, O. Auciello, H.-C. Yuan, Z. Ma, R. Carpick, D. Mancini, In *Micro-and Nanotechnology Sensors, Systems, and Applications*, volume 7318. SPIE, **2009** 314–320.

[92] J. Wang, J. Butler, T. Feygelson, C.-C. Nguyen, In *17th IEEE International Conference on Micro Electro Mechanical Systems. Maastricht MEMS 2004 Technical Digest.* **2004** 641–644.

[93] C. Goldsmith, A. Sumant, O. Auciello, J. Carlisle, H. Zeng, J. Hwang, C. Palego, W. Wang, R. Carpick, V. P. Adiga, A. Datta, C. Gudeman, S. O'Brien, S. Sampath, In *2010 IEEE MTT-S International Microwave Symposium.* **2010** 1–1.

[94] D. Rani, O. R. Opaluch, E. Neu, *Micromachines* **2020**, *12*, 1 36.

[95] A. N. Obraztsov, P. G. Kopylov, B. A. Loginov, M. A. Dolganov, R. R. Ismagilov, N. V. Savenko, *Review of Scientific Instruments* **2010**, *81*, 1, 013703.

[96] F. T. Tuyakova, E. A. Obraztsova, R. R. Ismagilov, *Journal of Nanophotonics* **2015**, *10*, 1 012517.

[97] Y. Tao, C. L. Degen, *Nano Letters* **2015**, *15*, 12 7893.

[98] M. Héritier, A. Eichler, Y. Pan, U. Grob, I. Shorubalko, M. D. Krass, Y. Tao, C. L. Degen, *Nano letters* **2018**, *18*, 3 1814.

[99] W. Zhao, N. Alcheikh, F. Khan, U. Yaqoob, M. Younis, *Sensors Actuators A: Physica* **2022**, *344* 113688.

[100] Y. Chen, L. Sang, S. Koizumi, Y. Koide, X. Liu, M. Liao, *Diamond Related Materials* **2022**, *129* 109340.

[101] M. K. Bhaskar, D. D. Sukachev, A. Sipahigil, R. E. Evans, M. J. Burek, C. T. Nguyen, L. J. Rogers, P. Siyushev, M. H. Metsch, H. Park, *Physical Review Letters* **2017**, *118*, 22 223603.

[102] M. J. Burek, Y. Chu, M. S. Liddy, P. Patel, J. Rochman, S. Meesala, W. Hong, Q. Quan, M. D. Lukin, M. Lončar, *Nature Communications* **2014**, *5*, 1 1.

[103] A. Socoliuc, E. Gnecco, S. Maier, O. Pfeiffer, A. Baratoff, R. Bennewitz, E. Meyer, *Science* **2006**, *313*, 5784 207.

[104] W. W. Jang, J. O. Lee, J.-B. Yoon, M.-S. Kim, J.-M. Lee, S.-M. Kim, K.-H. Cho, D.-W. Kim, D. Park, W.-S. Lee, *Applied Physics Letters* **2008**, *92*, 10 103110.

[105] H. Wu, L. Sang, Y. Li, T. Teraji, T. Li, M. Imura, J. You, Y. Koide, M. Toda, M. Liao, *Phys. Rev. Materials* **2018**, *2* 090601.

[106] I. Voiculescu, M. Liao, M. Zakerin, R. Berger, T. Ono, M. Toda, *Sensors and Actuators A: Physical* **2018**, *271* 356.

[107] Z. Zhang, Y. Wu, L. Sang, H. Wu, J. Huang, L. Wang, Y. Takahashi, R. Li, S. Koizumi, M. Toda, I. M. Akita, Y. Koide, M. Liao, *Materials Research Letters* **2020**, *8*, 5 180.

[108] Z. Zhang, H. Wu, L. Sang, Y. Takahashi, J. Huang, L. Wang, M. Toda, I. M. Akita, Y. Koide, S. Koizumi, M. Liao, *ACS Applied Materials & Interfaces* **2020**, *12*, 20 23155.

[109] B. Stipe, H. Mamin, T. Stowe, T. Kenny, D. Rugar, *Physical Review Letters* **2001**, *87*, 9 096801.

[110] A. Siria, T. Barois, K. Vilella, S. Perisanu, A. Ayari, D. Guillot, S. T. Purcell, P. Poncharal, *Nano Letters* **2012**, *12*, 7 3551.

[111] L. Du Preez, Ph.D. thesis, University of the Witwatersrand, Johannesburg, **1965**.

[112] J. H. N. Loubser, J. A. van Wyk, *Reports on Progress in Physics* **1978**, *41*, 8 1201.

[113] A. Gali, *Phys. Rev. B* **2009**, *79* 235210.

[114] M. V. Hauf, B. Grotz, B. Naydenov, M. Dankerl, S. Pezzagna, J. Meijer, F. Jelezko, J. Wrachtrup, M. Stutzmann, F. Reinhard, J. A. Garrido, *Phys. Rev. B* **2011**, *83* 081304.

[115] K. Beha, A. Batalov, N. B. Manson, R. Bratschitsch, A. Leitenstorfer, *Phys. Rev. Lett.* **2012**, *109* 097404.

[116] B. Grotz, M. V. Hauf, M. Dankerl, B. Naydenov, S. Pezzagna, J. Meijer, F. Jelezko, J. Wrachtrup, M. Stutzmann, F. Reinhard, J. A. Garrido, *Nature Communications* **2012**, *3*, 1 729.

[117] L. M. Pham, N. Bar-Gill, D. Le Sage, C. Belthangady, A. Stacey, M. Markham, D. J. Twitchen, M. D. Lukin, R. L. Walsworth, *Phys. Rev. B* **2012**, *86* 121202.

[118] C. D. Clark, C. A. Norris, *Journal of Physics C: Solid State Physics* **1971**, *4*, 14 2223.

[119] X.-F. He, N. B. Manson, P. T. H. Fisk, *Phys. Rev. B* **1993**, *47* 8809.

[120] X.-F. He, N. B. Manson, P. T. H. Fisk, *Phys. Rev. B* **1993**, *47* 8816.

[121] A. Gali, M. Fyta, E. Kaxiras, *Phys. Rev. B* **2008**, *77* 155206.

[122] F. M. Hossain, M. W. Doherty, H. F. Wilson, L. C. L. Hollenberg, *Phys. Rev. Lett.* **2008**, *101* 226403.

[123] M. W. Doherty, N. B. Manson, P. Delaney, L. C. L. Hollenberg, *New Journal of Physics* **2011**, *13*, 2 025019.

[124] A. Gruber, A. Dräbenstedt, C. Tietz, L. Fleury, J. Wrachtrup, C. von Borczyskowski, *Science* **1997**, *276*, 5321 2012.

[125] B. J. Maertz, A. P. Wijnheijmer, G. D. Fuchs, M. E. Nowakowski, D. D. Awschalom, *Applied Physics Letters* **2010**, *96*, 9, 092504.

[126] P. C. Maurer, J. R. Maze, P. L. Stanwix, L. Jiang, A. V. Gorshkov, A. A. Zibrov, B. Harke, J. S. Hodges, A. S. Zibrov, A. Yacoby, D. Twitchen, S. W. Hell, R. L. Walsworth, M. D. Lukin, *Nature Physics* **2010**, *6*, 11 912.

[127] A. Jarmola, V. M. Acosta, K. Jensen, S. Chemerisov, D. Budker, *Phys. Rev. Lett.* **2012**, *108* 197601.

[128] G. Davies, *Journal of Physics C: Solid State Physics* **1979**, *12*, 13 2551.

[129] L. J. Rogers, S. Armstrong, M. J. Sellars, N. B. Manson, *New Journal of Physics* **2008**, *10*, 10 103024.

[130] N. B. Manson, J. P. Harrison, M. J. Sellars, *Phys. Rev. B* **2006**, *74* 104303.

[131] A. Batalov, C. Zierl, T. Gaebel, P. Neumann, I.-Y. Chan, G. Balasubramanian, P. R. Hemmer, F. Jelezko, J. Wrachtrup, *Phys. Rev. Lett.* **2008**, *100* 077401.

[132] L. Robledo, H. Bernien, I. van Weperen, R. Hanson, *Phys. Rev. Lett.* **2010**, *105* 177403.

[133] T. Chakraborty, J. Zhang, D. Suter, *New Journal of Physics* **2017**, *19*, 7 073030.

[134] L. Robledo, L. Childress, H. Bernien, B. Hensen, P. F. A. Alkemade, R. Hanson, *Nature* **2011**, *477*, 7366 574.

[135] T. Luo, L. Lindner, J. Langer, V. Cimalla, X. Vidal, F. Hahl, C. Schreyvogel, S. Onoda, S. Ishii, T. Ohshima, D. Wang, D. A. Simpson, B. C. Johnson, M. Capelli, R. Blinder, J. Jeske, *New Journal of Physics* **2022**, *24*, 3 033030.

[136] V. M. Acosta, E. Bauch, M. P. Ledbetter, C. Santori, K.-M. C. Fu, P. E. Barclay, R. G. Beausoleil, H. Linget, J. F. Roch, F. Treussart, S. Chemerisov, W. Gawlik, D. Budker, *Phys. Rev. B* **2009**, *80* 115202.

[137] J. Schwartz, S. Aloni, D. F. Ogletree, T. Schenkel, *New Journal of Physics* **2012**, *14*, 4 043024.

[138] M. Mrzek, M. Schabikowski, M. Mitura-Nowak, J. Lekki, M. Marsza?ek, A. M. Wojciechowski, W. Gawlik, *Materials* **2021**, *14*, 4.

[139] Y. Shimotsuma, K. Kinouchi, R. Yanoshita, M. Fujiwara, N. Mizuochi, M. Uemoto, M. Shimizu, K. Miura, *Opt. Express* **2023**, *31*, 2 1594.

[140] Y. Liu, G. Chen, M. Song, X. Ci, B. Wu, E. Wu, H. Zeng, *Opt. Express* **2013**, *21*, 10 12843.

[141] F. Waldermann, P. Olivero, J. Nunn, K. Surmacz, Z. Wang, D. Jaksch, R. Taylor, I. Walmsley, M. Draganski, P. Reichart, A. Greentree, D. Jamieson, S. Prawer, *Diamond and Related Materials* **2007**, *16*, 11 1887.

[142] I. Aharonovich, C. Santori, B. A. Fairchild, J. Orwa, K. Ganesan, K.-M. C. Fu, R. G. Beausoleil, A. D. Greentree, S. Prawer, *Journal of Applied Physics* **2009**, *106*, 12, 124904.

[143] B. Naydenov, V. Richter, J. Beck, M. Steiner, P. Neumann, G. Balasubramanian, J. Achard, F. Jelezko, J. Wrachtrup, R. Kalish, *Applied Physics Letters* **2010**, *96*, 16, 163108.

[144] J. Martin, R. Wannemacher, J. Teichert, L. Bischoff, B. Köhler, *Applied Physics Letters* **1999**, *75*, 20 3096.

[145] K. Iakoubovskii, I. Kiflawi, K. Johnston, A. Collins, G. Davies, A. Stesmans, *Physica B: Condensed Matter* **2003**, *340* 67.

[146] T. Chakraborty, F. Lehmann, J. Zhang, S. Borgsdorf, N. Wöhrl, R. Remfort, V. Buck, U. Köhler, D. Suter, *Phys. Rev. Mater.* **2019**, *3* 065205.

[147] J. R. Maze, P. L. Stanwix, J. S. Hodges, S. Hong, J. M. Taylor, P. Cappellaro, L. Jiang, M. V. G. Dutt, E. Togan, A. S. Zibrov, A. Yacoby, R. L. Walsworth, M. D. Lukin, *Nature* **2008**, *455*, 7213 644.

[148] S. B. van Dam, M. Walsh, M. J. Degen, E. Bersin, S. L. Mouradian, A. Galiullin, M. Ruf, M. I-Jspeert, T. H. Taminiau, R. Hanson, D. R. Englund, *Phys. Rev. B* **2019**, *99* 161203.

[149] G. Balasubramanian, P. Neumann, D. Twitchen, M. Markham, R. Kolesov, N. Mizuochi, J. Isoya, J. Achard, J. Beck, J. Tissler, V. Jacques, P. R. Hemmer, F. Jelezko, J. Wrachtrup, *Nature Materials* **2009**, *8*, 5 383.

[150] B. D. Wood, G. A. Stimpson, J. E. March, Y. N. D. Lekhai, C. J. Stephen, B. L. Green, A. C. Frangeskou, L. Ginés, S. Mandal, O. A. Williams, G. W. Morley, *Phys. Rev. B* **2022**, *105* 205401.

[151] M. Wang, H. Sun, X. Ye, P. Yu, H. Liu, J. Zhou, P. Wang, F. Shi, Y. Wang, J. Du, *Science Advances* **2022**, *8*, 38 eabn9573.

[152] M. Kayci, J. Fan, O. Bakirman, A. Herrmann, *Proceedings of the National Academy of Sciences* **2021**, *118*, 51 e2112664118.

[153] G. P. Berman, A. R. Bishop, B. M. Chernobrod, M. E. Hawley, G. W. Brown, V. I. Tsifrinovich, *Journal of Physics: Conference Series* **2006**, *38*, 1 167.

[154] Z.-D. Zhang, S.-Y. Yin, L.-C. Wang, Y.-D. Wang, Y.-F. Li, Z.-N. Tian, Q.-D. Chen, *Opt. Express* **2022**, *30*, 18 32355.

[155] J.-C. Jaskula, E. Bauch, S. Arroyo-Camejo, M. D. Lukin, S. W. Hell, A. S. Trifonov, R. L. Walsworth, *Opt. Express* **2017**, *25*, 10 11048.

[156] A. Gruber, A. Dräbenstedt, C. Tietz, L. Fleury, J. Wrachtrup, C. von Borczyskowski, *Science* **1997**, *276*, 5321 2012.

[157] C. Kurtsiefer, S. Mayer, P. Zarda, H. Weinfurter, *Phys. Rev. Lett.* **2000**, *85* 290.

[158] J. Meijer, B. Burchard, M. Domhan, C. Wittmann, T. Gaebel, I. Popa, F. Jelezko, J. Wrachtrup, *Applied Physics Letters* **2005**, *87*, 26, 261909.

[159] J.-P. Tetienne, L. Rondin, P. Spinicelli, M. Chipaux, T. Debuisschert, J.-F. Roch, V. Jacques, *New Journal of Physics* **2012**, *14*, 10 103033.

[160] L. Robledo, H. Bernien, T. van der Sar, R. Hanson, *New Journal of Physics* **2011**, *13*, 2 025013.

[161] N. Alfasi, S. Masis, O. Shtempluck, E. Buks, *Phys. Rev. B* **2019**, *99* 214111.

[162] F. M. Stürner, Y. Liu, P.-O. Colard, M. Markham, F. Jelezko, *Applied Physics Letters* **2021**, *119*, 13, 134001.

[163] G. D. Fuchs, V. V. Dobrovitski, R. Hanson, A. Batra, C. D. Weis, T. Schenkel, D. D. Awschalom, *Phys. Rev. Lett.* **2008**, *101* 117601.

[164] M. Steiner, P. Neumann, J. Beck, F. Jelezko, J. Wrachtrup, *Phys. Rev. B* **2010**, *81* 035205.

[165] S. Felton, A. M. Edmonds, M. E. Newton, P. M. Martineau, D. Fisher, D. J. Twitchen, J. M. Baker, *Phys. Rev. B* **2009**, *79* 075203.

[166] A. Kiel, W. B. Mims, *Phys. Rev. B* **1972**, *5* 803.

[167] M. W. Doherty, N. B. Manson, P. Delaney, F. Jelezko, J. Wrachtrup, L. C. Hollenberg, *Physics Reports* **2013**, *528*, 1 1.

[168] E. Van Oort, M. Glasbeek, *Chemical Physics Letters* **1990**, *168*, 6 529.

[169] P. Neumann, R. Kolesov, V. Jacques, J. Beck, J. Tisler, A. Batalov, L. Rogers, N. B. Manson, G. Balasubramanian, F. Jelezko, J. Wrachtrup, *New Journal of Physics* **2009**, *11*, 1 013017.

[170] A. Batalov, V. Jacques, F. Kaiser, P. Siyushev, P. Neumann, L. J. Rogers, R. L. McMurtrie, N. B. Manson, F. Jelezko, J. Wrachtrup, *Phys. Rev. Lett.* **2009**, *102* 195506.

[171] T. X. Zhou, R. J. Stöhr, A. Yacoby, *Applied Physics Letters* **2017**, *111*, 16, 163106.

[172] L. Rondin, J.-P. Tetienne, S. Rohart, A. Thiaville, T. Hingant, P. Spinicelli, J.-F. Roch, V. Jacques, *Nature Communications* **2013**, *4*, 1 2279.

[173] P. Appel, M. Ganzhorn, E. Neu, P. Maletinsky, *New Journal of Physics* **2015**, *17*, 11 112001.

[174] W. Lei, G. Hao, C. Yu-Lei, W. Da-Jin, Z. Rui, L. Wen-Yao, L. Chun-Ming, X. Mei-Jing, Z. Bin-Bin, Z. Qiang, T. Jun, L. Jun, *Acta Physica Sinica* **2018**, *67*, 4 047601.

[175] Z. Qiu, A. Hamo, U. Vool, T. X. Zhou, A. Yacoby, *npj Quantum Information* **2022**, *8*, 1 107.

[176] B. D. Mangum, E. Shafran, C. Mu, J. M. Gerton, *Nano Letters* **2009**, *9*, 10 3440.

[177] P. Rabl, *Phys. Rev. B* **2010**, *82* 165320.

[178] J. R. Maze, A. Gali, E. Togan, Y. Chu, A. Trifonov, E. Kaxiras, M. D. Lukin, *New Journal of Physics* **2011**, *13*, 2 025025.

[179] F. Dolde, H. Fedder, M. W. Doherty, T. Nöbauer, F. Rempp, G. Balasubramanian, T. Wolf, F. Reinhard, L. C. L. Hollenberg, F. Jelezko, J. Wrachtrup, *Nature Physics* **2011**, *7*, 6 459.

[180] J. Teissier, A. Barfuss, P. Appel, E. Neu, P. Maletinsky, *Phys. Rev. Lett.* **2014**, *113* 020503.

[181] G. de Lange, Z. H. Wang, D. Ristè, V. V. Dobrovitski, R. Hanson, *Science* **2010**, *330*, 6000 60.

[182] M. W. Doherty, V. V. Struzhkin, D. A. Simpson, L. P. McGuinness, Y. Meng, A. Stacey, T. J. Karle, R. J. Hemley, N. B. Manson, L. C. L. Hollenberg, S. Prawer, *Phys. Rev. Lett.* **2014**, *112* 047601.

[183] A. Awadallah, I. Zohar, A. Finkler, *Journal of Applied Physics* **2023**, *133*, 14, 145103.

[184] S. D. Bennett, N. Y. Yao, J. Otterbach, P. Zoller, P. Rabl, M. D. Lukin, *Phys. Rev. Lett.* **2013**, *110* 156402.

[185] E. R. MacQuarrie, M. Otten, S. K. Gray, G. D. Fuchs, *Nature Communications* **2017**, *8*, 1 14358.

[186] H. Chen, N. F. Opondo, B. Jiang, E. R. MacQuarrie, R. S. Daveau, S. A. Bhave, G. D. Fuchs, *Nano Letters* **2019**, *19*, 10 7021, pMID: 31498998.

[187] H. Y. Chen, S. A. Bhave, G. D. Fuchs, *Phys. Rev. Appl.* **2020**, *13* 054068.

[188] H. Y. Chen, S. A. Bhave, G. D. Fuchs, *Phys. Rev. Appl.* **2020**, *13* 054068.

[189] M. J. A. Schuetz, E. M. Kessler, G. Giedke, L. M. K. Vandersypen, M. D. Lukin, J. I. Cirac, *Phys. Rev. X* **2015**, *5* 031031.

[190] M. Tabib-Azar, In *2022 IEEE Sensors*. **2022** 1–4.

[191] A. Golter, T. Oo, M. Amezcua, H. Wang, In *Photonics and Fiber Technology 2016 (ACOFT, BGPP, NP)*. Optica Publishing Group, **2016** NW3A.7.

[192] D. A. Golter, T. Oo, M. Amezcua, I. Lekavicius, K. A. Stewart, H. Wang, *Phys. Rev. X* **2016**, *6* 041060.

[193] P.-B. Li, Y. Zhou, W.-B. Gao, F. Nori, *Phys. Rev. Lett.* **2020**, *125* 153602.

[194] P. Kehayias, M. J. Turner, R. Trubko, J. M. Schloss, C. A. Hart, M. Wesson, D. R. Glenn, R. L. Walsworth, *Phys. Rev. B* **2019**, *100* 174103.

[195] K. Xia, J. Twamley, *Phys. Rev. B* **2016**, *94* 205118.

[196] K. V. Kepesidis, S. D. Bennett, S. Portolan, M. D. Lukin, P. Rabl, *Phys. Rev. B* **2013**, *88* 064105.

[197] L. Giannelli, R. Betzholz, L. Kreiner, M. Bienert, G. Morigi, *Phys. Rev. A* **2016**, *94* 053835.

[198] P. Rabl, S. J. Kolkowitz, F. H. L. Koppens, J. G. E. Harris, P. Zoller, M. D. Lukin, *Nature Physics* **2010**, *6*, 8 602.

[199] K. S. Thorne, R. W. Drever, C. M. Caves, M. Zimmermann, V. D. Sandberg, *Physical Review Letters* **1978**, *40*, 11 667.

[200] M. Aspelmeyer, T. J. Kippenberg, F. Marquardt, *Reviews of Modern Physics* **2014**, *86*, 4 1391.

[201] S. Weis, R. Rivière, S. Deléglise, E. Gavartin, O. Arcizet, A. Schliesser, T. J. Kippenberg, *Science* **2010**, *330*, 6010 1520.

[202] F. Hocke, X. Zhou, A. Schliesser, T. J. Kippenberg, H. Huebl, R. Gross, *New Journal of Physics* **2012**, *14*, 12 123037.

[203] Y. Liu, Q. Liu, S. Wang, Z. Chen, M. A. Sillanpää, T. Li, *Physical Review Letters* **2021**, *127*, 27 273603.

[204] F. Monifi, J. Zhang, Ş. K. Özdemir, B. Peng, Y.-x. Liu, F. Bo, F. Nori, L. Yang, *nature photonics* **2016**, *10*, 6 399.

[205] J. Li, Z.-H. Zhou, S. Wan, Y.-L. Zhang, Z. Shen, M. Li, C.-L. Zou, G.-C. Guo, C.-H. Dong, *Physical Review Letters* **2022**, *129*, 6 063605.

[206] T. Kuang, R. Huang, W. Xiong, Y. Zuo, X. Han, F. Nori, C.-W. Qiu, H. Luo, H. Jing, G. Xiao, *Nature Physics* **2023**, 1–6.

[207] D. Mason, J. Chen, M. Rossi, Y. Tsaturyan, A. Schliesser, *Nature Physics* **2019**, *15*, 8 745.

[208] T. P. Purdy, R. W. Peterson, C. Regal, *Science* **2013**, *339*, 6121 801.

[209] Y. Liu, J. Mummery, J. Zhou, M. A. Sillanpää, *Physical Review Applied* **2021**, *15*, 3 034004.

[210] S. Barzanjeh, A. Xuereb, S. Gröblacher, M. Paternostro, C. A. Regal, E. M. Weig, *Nature Physics* **2022**, *18*, 1 15.

[211] A. Clerk, K. Lehnert, P. Bertet, J. Petta, Y. Nakamura, *Nature Physics* **2020**, *16*, 3 257.

[212] G. Kurizki, P. Bertet, Y. Kubo, K. Mølmer, D. Petrosyan, P. Rabl, J. Schmiedmayer, *Proceedings of the National Academy of Sciences* **2015**, *112*, 13 3866.

[213] E. E. Wollman, C. Lei, A. Weinstein, J. Suh, A. Kronwald, F. Marquardt, A. A. Clerk, K. Schwab, *Science* **2015**, *349*, 6251 952.

[214] J.-M. Pirkkalainen, E. Damskägg, M. Brandt, F. Massel, M. A. Sillanpää, *Physical Review Letters* **2015**, *115*, 24 243601.

[215] F. Lecocq, J. B. Clark, R. W. Simmonds, J. Aumentado, J. D. Teufel, *Physical Review X* **2015**, *5*, 4 041037.

[216] T. Palomaki, J. Teufel, R. Simmonds, K. W. Lehnert, *Science* **2013**, *342*, 6159 710.

[217] R. Riedinger, S. Hong, R. A. Norte, J. A. Slater, J. Shang, A. G. Krause, V. Anant, M. Aspelmeyer, S. Gröblacher, *Nature* **2016**, *530*, 7590 313.

[218] C. Ockeloen-Korppi, E. Damskägg, G.-S. Paraoanu, F. Massel, M. Sillanpää, *Physical review letters* **2018**, *121*, 24 243601.

[219] S. Barzanjeh, E. Redchenko, M. Peruzzo, M. Wulf, D. Lewis, G. Arnold, J. M. Fink, *Nature* **2019**, *570*, 7762 480.

[220] R. Riedinger, A. Wallucks, I. Marinković, C. Löschnauer, M. Aspelmeyer, S. Hong, S. Gröblacher, *Nature* **2018**, *556*, 7702 473.

[221] C. Ockeloen-Korppi, E. Damskägg, J.-M. Pirkkalainen, M. Asjad, A. Clerk, F. Massel, M. Woolley, M. Sillanpää, *Nature* **2018**, *556*, 7702 478.

[222] S. Hong, R. Riedinger, I. Marinković, A. Wallucks, S. G. Hofer, R. A. Norte, M. Aspelmeyer, S. Gröblacher, *Science* **2017**, *358*, 6360 203.

[223] I. Marinković, A. Wallucks, R. Riedinger, S. Hong, M. Aspelmeyer, S. Gröblacher, *Physical review letters* **2018**, *121*, 22 220404.

[224] L. Mercier de Lépinay, C. F. Ockeloen-Korppi, M. J. Woolley, M. A. Sillanpää, *Science* **2021**, *372*, 6542 625.

[225] S. Kotler, G. A. Peterson, E. Shojaee, F. Lecocq, K. Cicak, A. Kwiatkowski, S. Geller, S. Glancy, E. Knill, R. W. Simmonds, et al., *Science* **2021**, *372*, 6542 622.

[226] A. Bassi, K. Lochan, S. Satin, T. P. Singh, H. Ulbricht, *Reviews of Modern Physics* **2013**, *85*, 2 471.

[227] A. Matsumura, K. Yamamoto, *Physical Review D* **2020**, *102*, 10 106021.

[228] T. Westphal, H. Hepach, J. Pfaff, M. Aspelmeyer, *Nature* **2021**, *591*, 7849 225.

[229] T. Krisnanda, G. Y. Tham, M. Paternostro, T. Paterek, *npj Quantum Information* **2020**, *6*, 1 1.

[230] K. Stannigel, P. Rabl, A. S. Sørensen, M. Lukin, P. Zoller, *Physical Review A* **2011**, *84*, 4 042341.

[231] R. Delaney, M. Urmey, S. Mittal, B. Brubaker, J. Kindem, P. Burns, C. Regal, K. Lehnert, *Nature* **2022**, *606*, 7914 489.

[232] Y. Chu, S. Gröblacher, *Applied Physics Letters* **2020**, *117*, 15 150503.

[233] N. J. Lambert, A. Rueda, F. Sedlmeir, H. G. Schwefel, *Advanced Quantum Technologies* **2020**, *3*, 1 1900077.

[234] N. Lauk, N. Sinclair, S. Barzanjeh, J. P. Covey, M. Saffman, M. Spiropulu, C. Simon, *Quantum Science and Technology* **2020**, *5*, 2 020501.

[235] B. Khanaliloo, H. Jayakumar, A. C. Hryciw, D. P. Lake, H. Kaviani, P. E. Barclay, *Phys. Rev. X* **2015**, *5* 041051.

[236] H. Jayakumar, B. Khanaliloo, D. P. Lake, P. E. Barclay, *Physical Review Applied* **2021**, *16*, 1 014063.

[237] M. Mitchell, B. Khanaliloo, D. P. Lake, T. Masuda, J. P. Hadden, P. E. Barclay, *Optica* **2016**, *3*, 9 963.

[238] M. Mitchell, D. P. Lake, P. E. Barclay, *Optica* **2019**, *6*, 7 832.

[239] D. P. Lake, M. Mitchell, B. C. Sanders, P. E. Barclay, *Nature Communications* **2020**, *11*, 1 2208.

[240] D. P. Lake, M. Mitchell, D. D. Sukachev, P. E. Barclay, *Nature communications* **2021**, *12*, 1 663.

[241] M. J. Burek, J. D. Cohen, S. M. Meenehan, N. El-Sawah, C. Chia, T. Ruelle, S. Meesala, J. Rochman, H. A. Atikian, M. Markham, et al., *Optica* **2016**, *3*, 12 1404.

[242] P. K. Shandilya, D. P. Lake, M. J. Mitchell, D. D. Sukachev, P. E. Barclay, *Nature Physics* **2021**, *17*, 12 1420.

[243] J. V. Cady, O. Michel, K. W. Lee, R. N. Patel, C. J. Sarabalis, A. H. Safavi-Naeini, A. C. B. Jayich, *Quantum Science and Technology* **2019**, *4*, 2 024009.

[244] Y. Tsaturyan, A. Barg, E. S. Polzik, A. Schliesser, *Nature Nanotechnology* **2017**, *12*, 8 776.

[245] A. H. Ghadimi, S. A. Fedorov, N. J. Engelsen, M. J. Bereyhi, R. Schilling, D. J. Wilson, T. J. Kippenberg, *Science* **2018**, *360*, 6390 764.

[246] S. A. Fedorov, A. Beccari, N. J. Engelsen, T. J. Kippenberg, *Phys. Rev. Lett.* **2020**, *124* 025502.

[247] S. A. Fedorov, N. J. Engelsen, A. H. Ghadimi, M. J. Bereyhi, R. Schilling, D. J. Wilson, T. J. Kippenberg, *Phys. Rev. B* **2019**, *99* 054107.

[248] X. Li, I. Lekavicius, H. Wang, *Nano Letters* **2022**, *22*, 24 10163, pMID: 36515668.

[249] A. Lenef, S. C. Rand, *Phys. Rev. B* **1996**, *53* 13441.

[250] M. W. Doherty, J. Michl, F. Dolde, I. Jakobi, P. Neumann, N. B. Manson, J. Wrachtrup, *New Journal of Physics* **2014**, *16*, 6 063067.

[251] L. Rondin, J.-P. Tetienne, P. Spinicelli, C. Dal Savio, K. Karrai, G. Dantelle, A. Thiaville, S. Rohart, J.-F. Roch, V. Jacques, *Applied Physics Letters* **2012**, *100*, 15, 153118.

[252] L. T. Hall, C. D. Hill, J. H. Cole, B. Städler, F. Caruso, P. Mulvaney, J. Wrachtrup, L. C. L. Hollenberg, *Proceedings of the National Academy of Sciences* **2010**, *107*, 44 18777.

[253] J. Tisler, T. Oeckinghaus, R. J. Stöhr, R. Kolesov, R. Reuter, F. Reinhard, J. Wrachtrup, *Nano Letters* **2013**, *13*, 7 3152, pMID: 23795752.

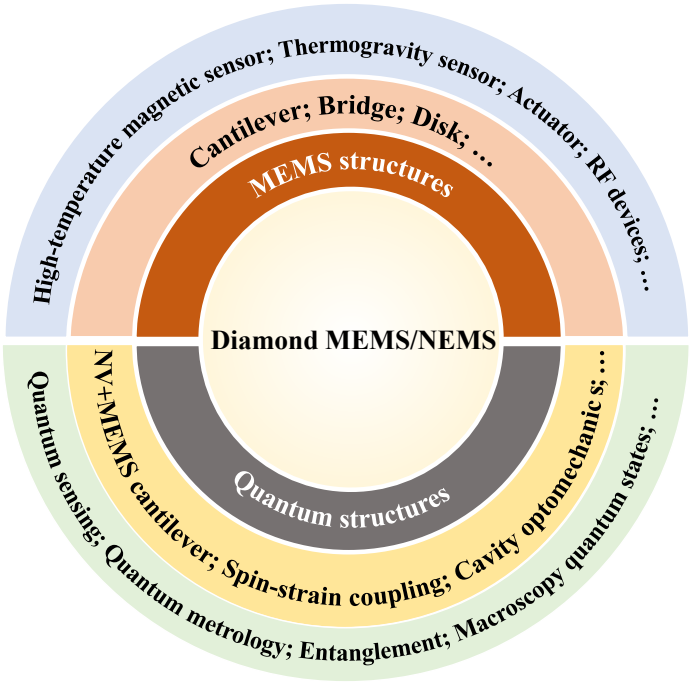

Figure 1: An overview of diamond MEMS/NEMS devices for applications in the classical and quantum domains.

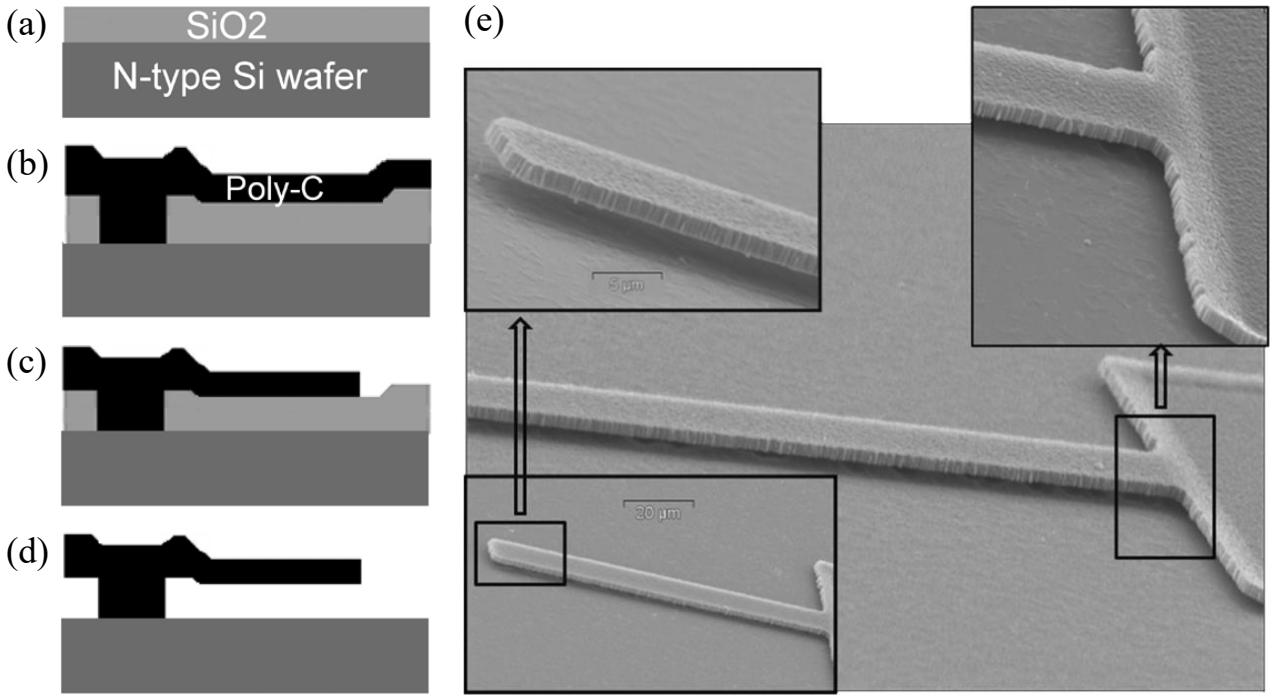

Figure 2: Fabrication process flow of MCD-based MEMS resonators. a) SiO_2/Si substrate. b) SiO_2 patterning and MCD deposition. c) MCD patterning. d) Cantilever structure release. d) SEM images of MCD-based cantilevers. Reproduced with permission.[43] Copyright 2008, IEEE.

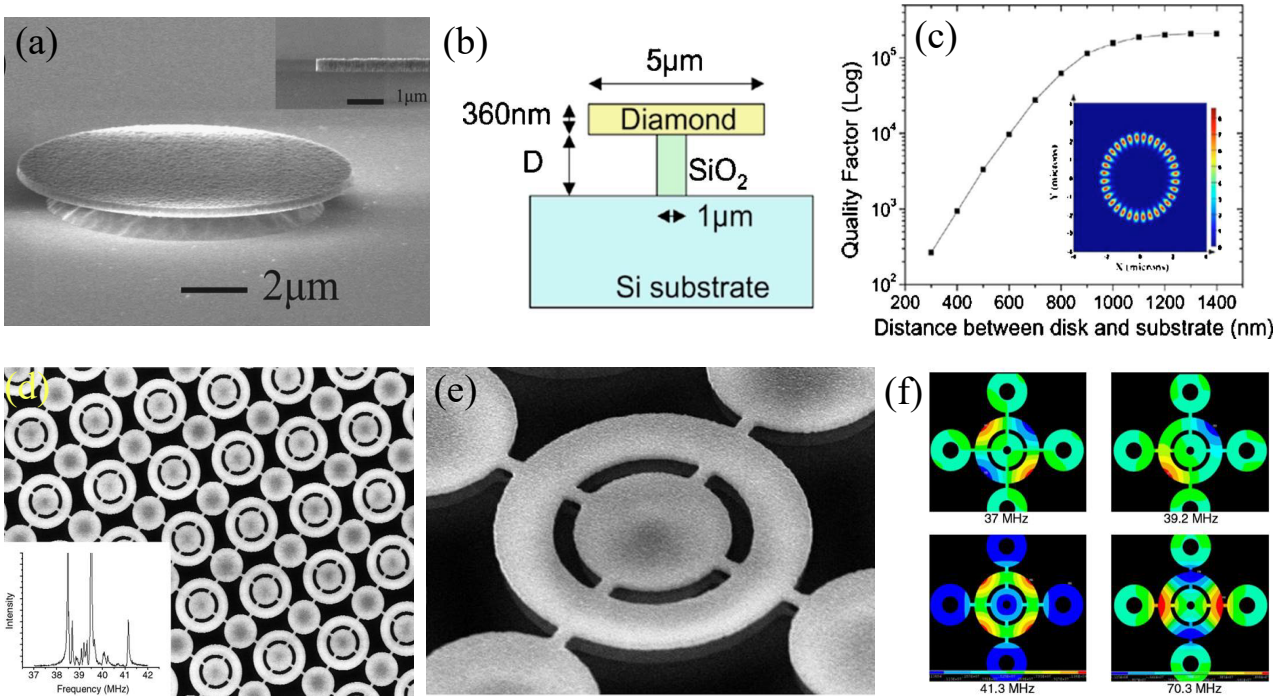

Figure 3: a) SEM image of a NCD microdisk with 10 μm in diameter. b) Side view of a NCD microdisk structure used for simulation. D is the distance between the disk and substrate. c) Q vs D obtained by three-dimensional finite-difference time-domain (FDTD) simulation. Reproduced with permission.[87] Copyright 2007, American Institute of Physics. d) SEM image of NCD resonators array. The width and thickness of a ring resonator are 1.5 μm and 100 nm, respectively. Inset: Band formation resulting from the coupling of individual resonators in 2D array. e) SEM image of one unit cell for NCD resonator array with the 48° inclination. The resonance frequency of the ring resonator is 40.18 MHz and the Q factor is 5 000. f) Modal analysis of the NCD resonator array unit cell. Reproduced with permission.[52] Copyright 2006, Elsevier.

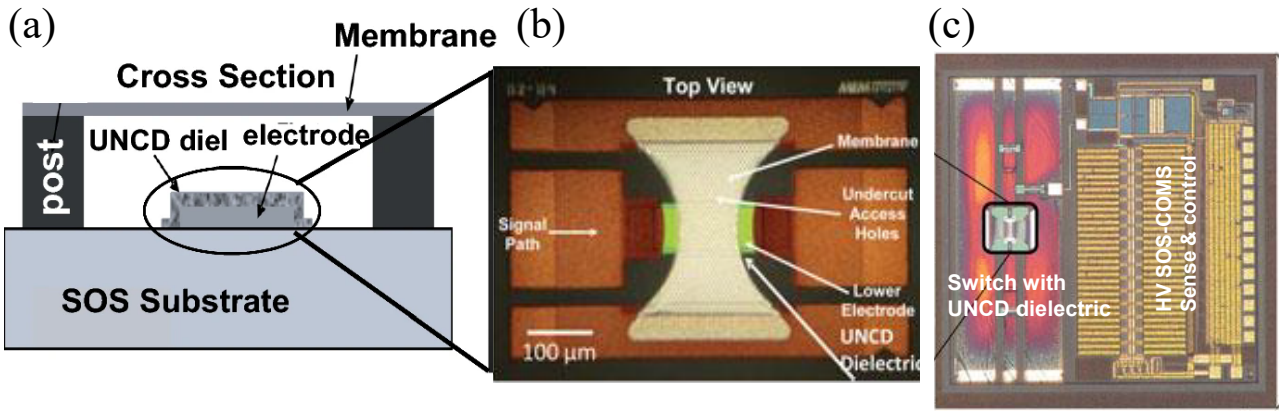

Figure 4: a) Cross-section structure of RF-MEMS capacitive switch with UNCD dielectric layer on metal (W) electrode and metal membrane. b) Optical image of an RF-MEMS switch with the metallic membrane and the UNCD dielectric layer. c) Optical image of a single integrated RF-UNCD/MEMS switch/SOS-CMOS device. Reproduced with permission.[93] Copyright 2010, SPIE.

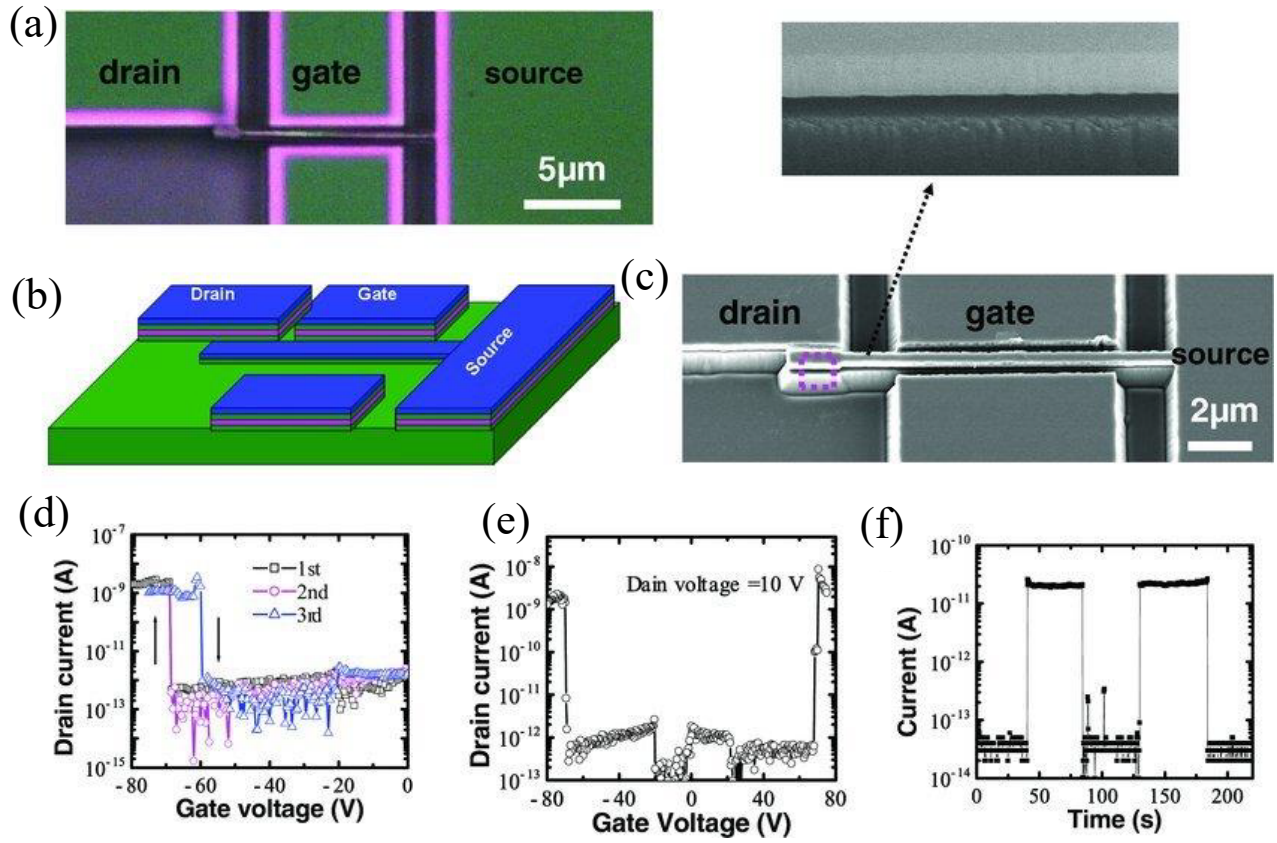

Figure 5: a) Optical image of the SCD NEMS switch. b) Schematic image of the SCD NEMS switch. c) SEM image of the switch viewed at a titled angle of 20°. d) Repeated and hysteresis switching behavior of the device controlled by the gate voltage. e) Gate voltage-drain current dependence of a similar switch. f) Transient switching behavior of the switch at a gate voltage of 75 V and a drain voltage of 5 V. Reproduced with permission.[14] Copyright 2010, Wiley.

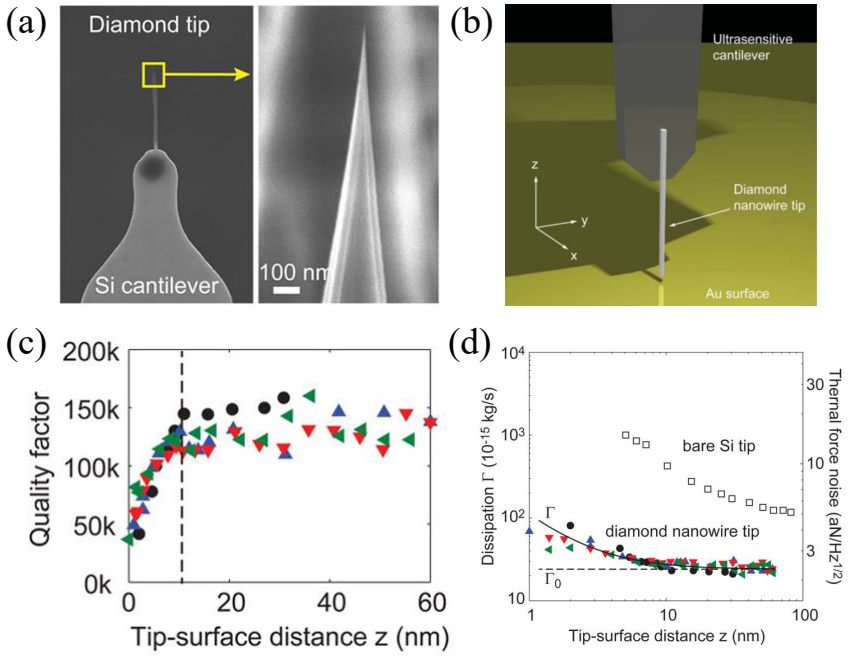

Figure 6: a) SEM image of integration of a SCD nanowire tips on a silicon cantilever. b) Schematic illustration of the experimental configuration of the SCD-tipped silicon cantilever oscillates along x over a gold surface in a pendulum geometry. c) Dependence of Q factor on the distance, z from the SCD nanowire tip to the Au surface. d) Mechanical dissipation and thermal force noise spectral density as a function of z. The dashed line indicates the intrinsic dissipation of $\Gamma_0 = 24 \times 10^{-15}$ kg/s. Reproduced with the permission.[97] Copyright 2015 American Chemical Society.

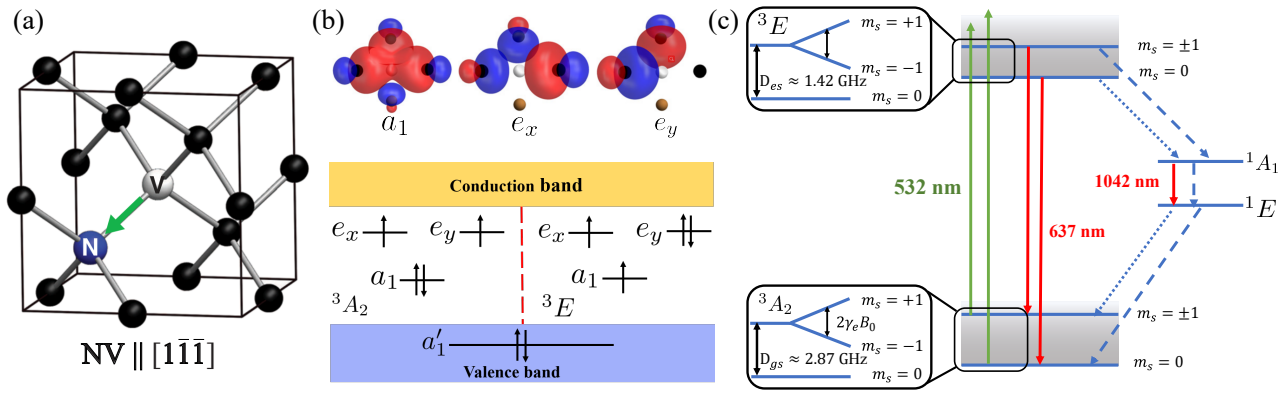

Figure 7: a) Atomic structures of NV center consisted of a substitutive nitrogen atom and adjacent vacancy. Carbon atoms are depicted in black, nitrogen atom in blue, and vacancy in grey. Reproduced with permission.[117] Copyright 2012, AP-S. b) The molecular orbits (top) and the electrons occupation of defects level of ground state $^3A_2$ and excited state ^3E (bottom). Reproduced with permission.[249, 123] Copyright 1996, APS. c) Schematic of the electronic structure of NV^-, including Zeeman shifts of the electron spin states m_s related to magnetic field. The non-resonant excitation of laser at 532 nm is shown as green arrows, and the spontaneous emission at 637 and 1042 nm is depicted as red arrows. The intermediate singlet states, represented by $^1A_1$ and ^1E, are shown, with non-radiative transitions indicated by dashed lines and dotted lines, respectively. The intensity of decay rate showed by the dashed lines are faster than that of dotted lines. The zero-field splitting and the effect of magnetic field are shown in zoom figures. Reproduced with permission.[250] Copyright 2013, Elsevier.

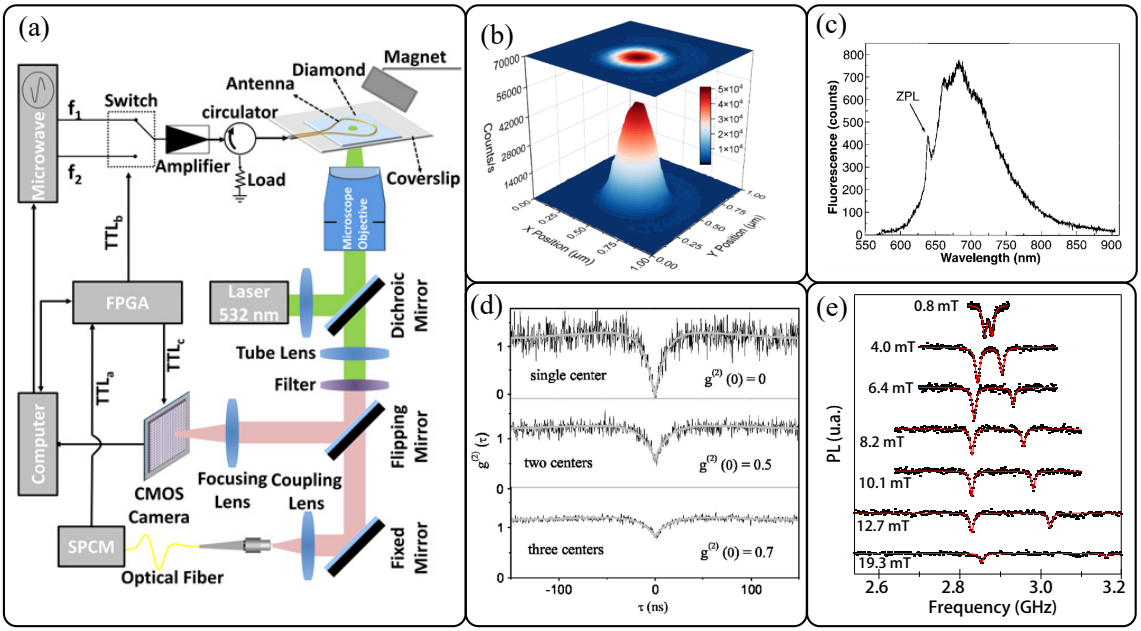

Figure 8: a) Schematic of the experimental setup used for the ODMR measurements with NV centers. Reproduced with permission.[152] Copyright 2021, United States National Academy of Sciences. b) Single NV center fluorescence scanning image. Reproduced with permission.[154] Copyright 2022, Optica Publishing Group. c) Fluorescence spectrum of a single NV center. The zero phonon line (ZPL) is illustrated at 637 nm of wavelength. Reproduced with permission.[156] Copyright 1997, AAAS. d) Normalized fluorescence intensity autocorrelation function of different NV spots. The curves have been corrected for background contributions. Reproduced with permission.[158] Copyright 2005, American Institute of Physics. e) Example of optically detected magnetic resonance on a single NV center in a bulk diamond, where the magnetic field is applied with an angle $\theta = 74°$ with respect to the NV axis. Reproduced with permission.[159] Copyright 2012, IOP Publishing Ltd.

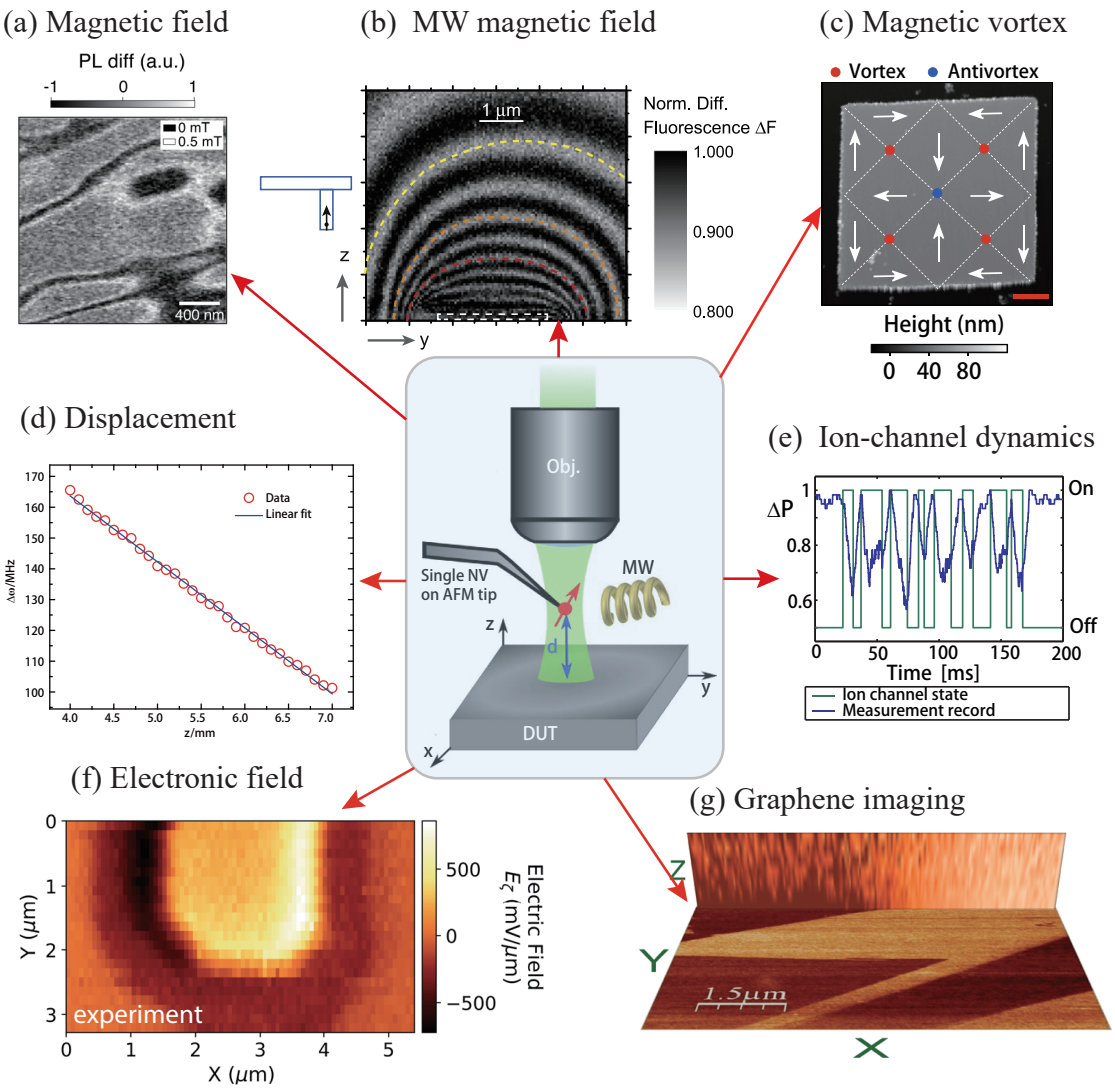

Figure 9: Centered: Schematic of NV center-based scanning spin microscope. The single NV defect in the cantilever serves as an ultrasensitive magnetometer with a spatial resolution at the nanometer scale. Changes in the EPR frequency of the NV center can be detected optically due to the interaction between the NV center and the device under test (DUT). Reproduced with permission.[172] Copyright 2013, Nature Publishing Group. a) A dual iso-magnetic field image of a commercial hard disk was obtained by measuring the PL difference for two consecutively fixed MW frequencies. Dark and bright areas depict the magnetic field with $|B_z = 0|$ and $|B_z = 0.5|$ mT, respectively. Reproduced with permission.[251] Copyright 2012, American Institute of Physics. b) The isofield imaging of an MW magnetic field. Reproduced with permission.[173] Copyright 2015, IOP Publishing Ltd. (c) AFM image of the square of $Fe_{20}Ni_{80}$ with a thickness of 50 nm and a 5 μm side length. The white arrows depict the higher-energy magnetization structure, with four magnetic vortices (red dots) distributed around one anti-vortex at the centre (blue dot). Reproduced with permission.[172] Copyright 2013, Nature Publishing Group. d) Zeeman splitting at different positions along the z axis. Reproduced with permission.[174] Copyright 2018, Chinese Physical Society. e) Fluorescence changes as ions flow across the cell membrane surface, which permits the temporal tracking of ion-channel dynamics. Reproduced with permission.[252] Copyright 2010, National Academy of Sciences. f) A two-dimensional map of the AC electric field distribution in the U-shaped Au structure. Reproduced with permission.[175] Copyright 2022, Nature Partner Journals. g) Three dimensional near-field image of fluorescence resonance energy transfer (FRET) in multilayer graphene. Reproduced with permission.[253] Copyright 2013, American Chemical Society.

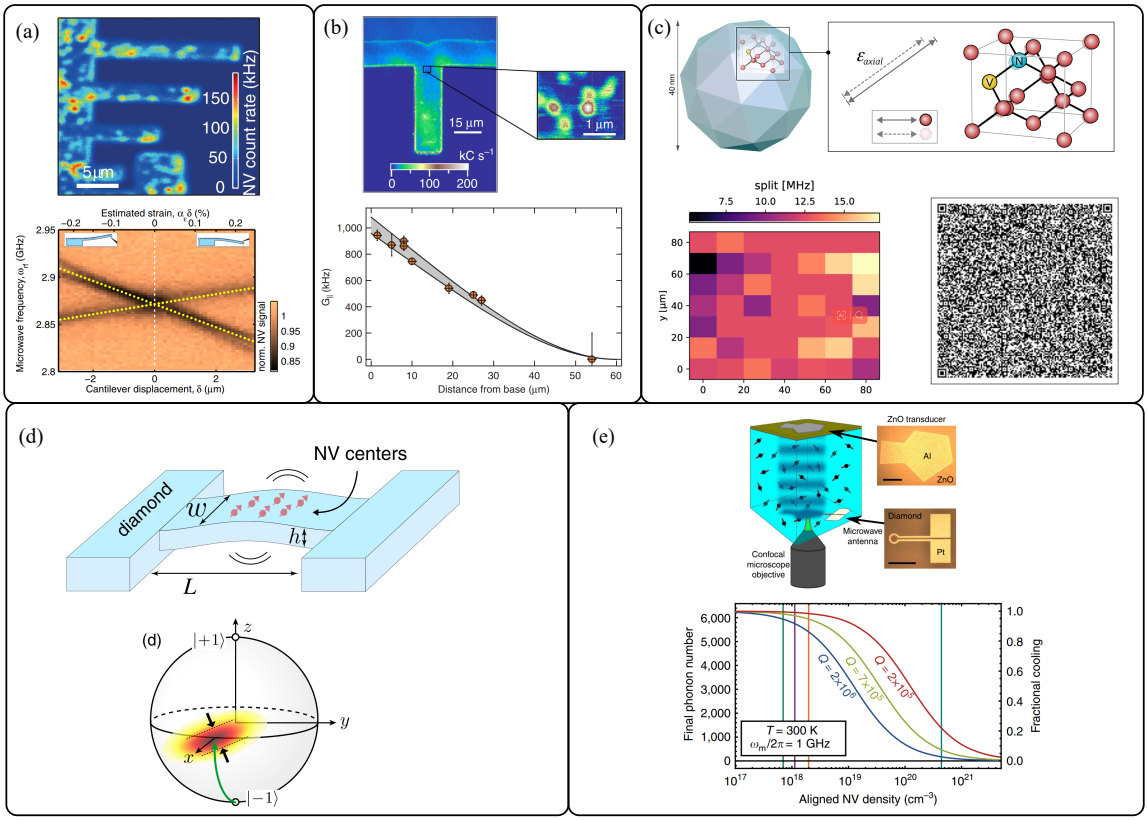

Figure 10: Demonstrations of spin-strain coupling of NV centers in diamond. a) Top: Confocal image of the cantilever with individual, implanted NV centers scattered across the sample surface. Bottom: Strain splitting of NV ESR lines as a function of static cantilever displacement. Positive and negative values of δ correspond to two different data sets (separated by the dashed line) and represent tensile and compressive strain at the NV location, respectively (see insets). Reproduced with permission.[180] Copyright 2014, American Physical Society; b) Top: Confocal image of a cantilever showing the presence of single embedded NV centres. Bottom: Measured strain coupling as a function of the NV's distance from the cantilever base for a fixed oscillation amplitude, the grey shaded area shows the region of expected strain couplings from theory. Reproduced with permission.[28] Copyright 2014, Nature Publishing Group; c) Top: A sketch of the diamond lattice with an NV center, defining the direction of the strain field along the NV axis and perpendicular to it. The strain parameters distribution of a collection of nanodiamonds dispersed on a glass substrate (left bottom), along with the a machine-readable qrcode that includes the strain distribution of each NV centers (right bottom). Reproduced with permission.[183] Copyright 2023, American Institute of Physics; d) Top: All-diamond doubly clamped mechanical resonator with an ensemble of embedded NV centers. Bottom: Squeezing of the spin uncertainty distribution of an NV ensemble. Reproduced with permission.[184] Copyright 2013, American Physical Society. e) Top: The spin-strain coupling through the bulk acoustic wave, in which the piezoelectric materials ZnO is used to generate the mechanical vibration. Bottom: Final phonon number achieved by the cooling protocol as a function of the density of properly aligned NV centers. Reproduced with permission.[185] Copyright 2014, Nature Publishing Group.

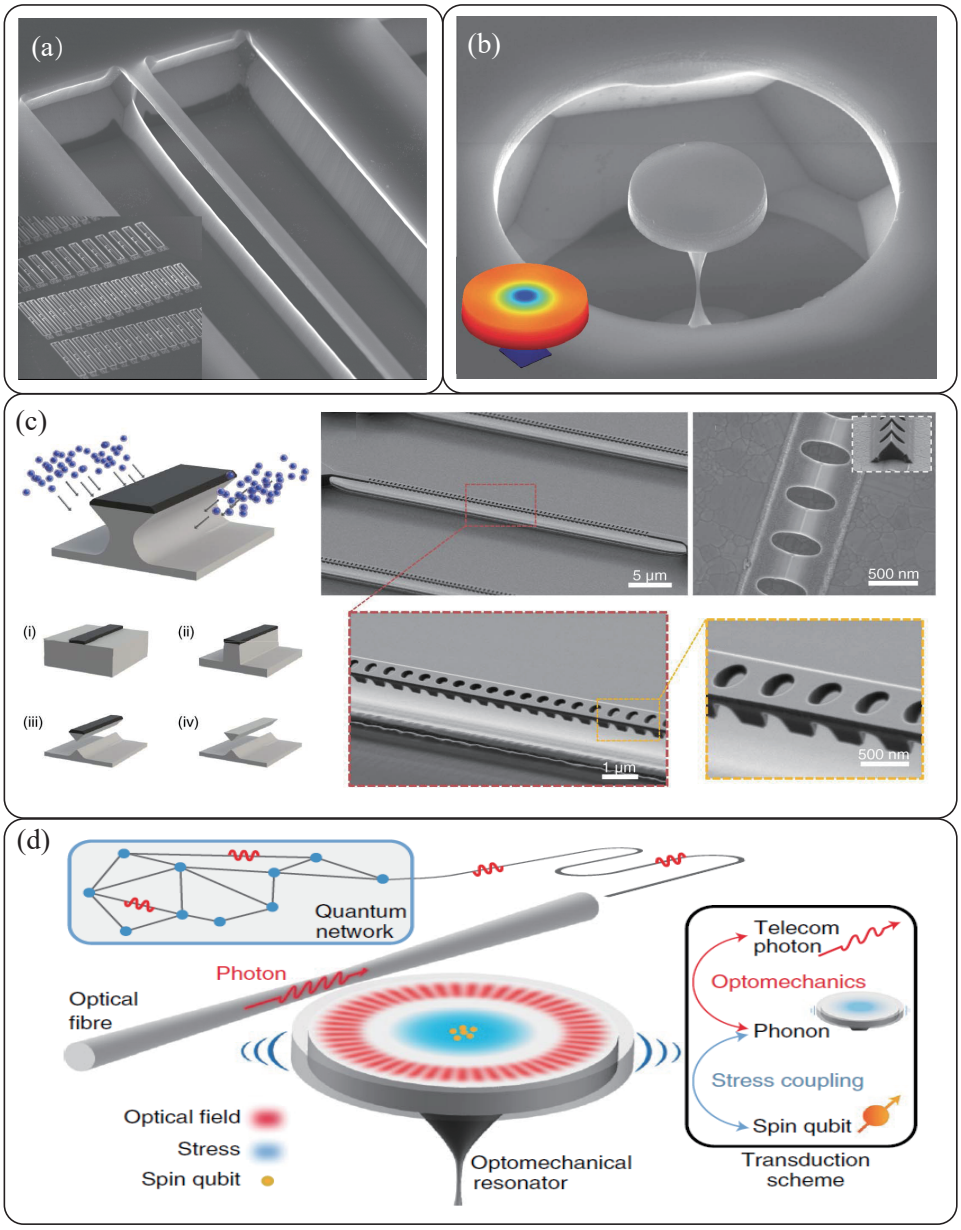

Figure 11: The cavity optomechanical device with diamond mechanical resonators. a) SEM image of the nanobeam waveguide-optomechanical system made of single crystal diamond material. Reproduced with permission.[235] Copyright 2015, APS. b) SEM image of diamond microdisk with a 5 μm diameter. The minimum pedestal width of this device is of 100 nm. Reproduced with permission.[237] Copyright 2016, Optica Publishing Group. c) The diamond optomechanical crystal and its fabrication recipe which is consist of (i) defining an etch mask on a substrate via EBL, (ii) transferring etch mask pattern onto the substrate by plasma etching, (iii) employing angled etching to realize suspended nanobeam structures, and (iv) removing residual etch mask. Reproduced with permission.[241] Copyright 2016, Optica Publishing Group. d) Spin quantum memory for photons at communication wavelengths. Transport of quantum states using microdisk cavity optomechanical quantum coherent interfaces. The inset shows a scheme for state transfer (right) and a conceptual diagram of a future large-scale quantum network (left). The quantum state mainly converts the transmitted communication band photons into mechanical vibrations of the diamond microdisk through the microdisk interface, and then converts the coherent mechanical vibrations (phonons) to spins through stress and strain and stores quantum information. Reproduced with permission.[242] Copyright 2021, Nature Publishing Group.

Table of Contents

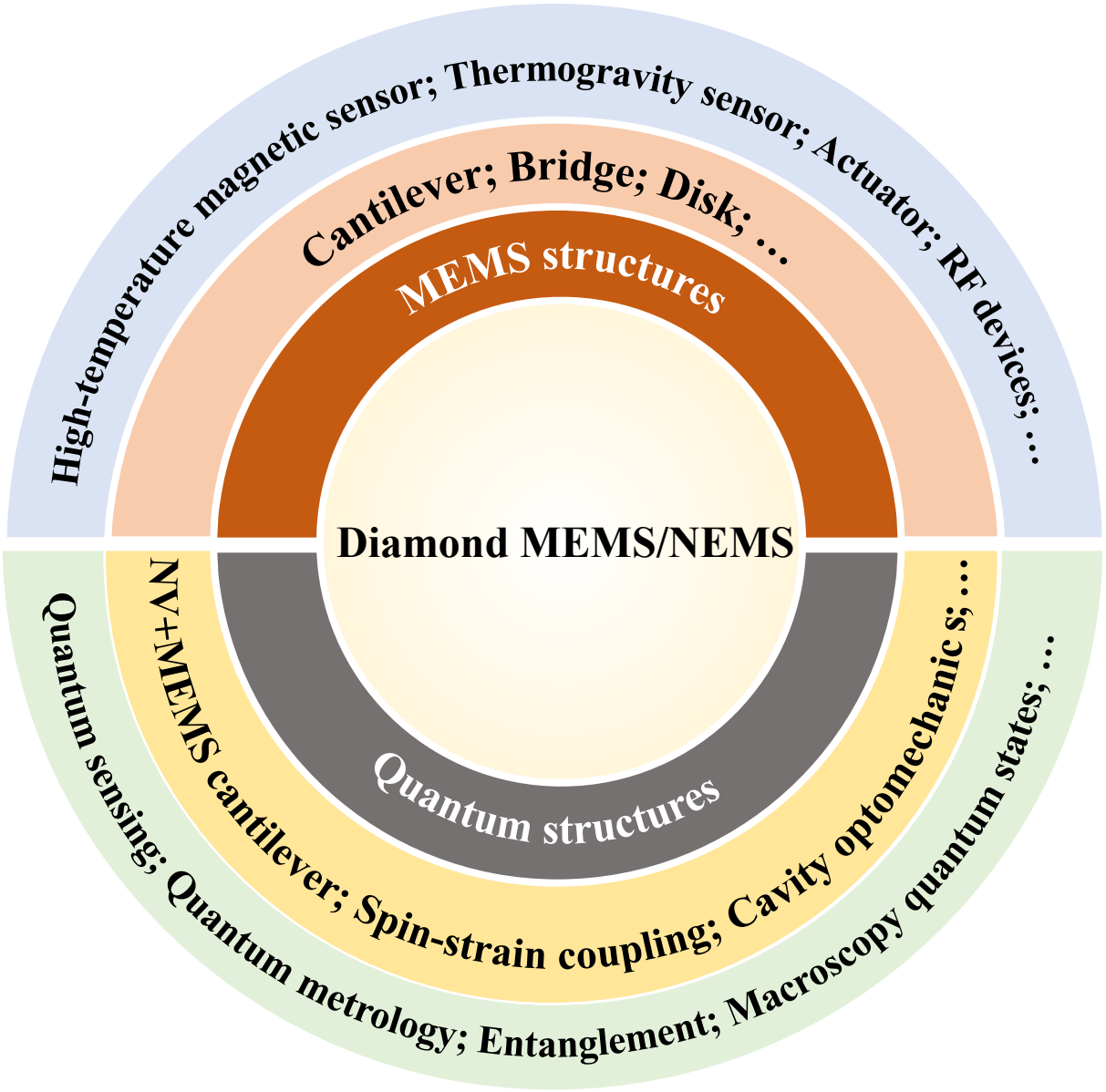

An overview of diamond MEMS/NEMS and the applications in classical and quantum domains. Classical applications encompass a wide range of practical applications such as sensors, actuators, and RF devices. The potential applications in quantum realm involve the hybrid system of AFM cantilevers embedded with NV centers, the strain-NV modulation, and the quantum network based phonon-photon-spin interactions.